©ESO 2018

Multiple Star Systems in the Orion Nebula

GRAVITY collaboration[*]: Martina Karl[**,1], Oliver Pfuhl[***,1], Frank Eisenhauer[1], Reinhard Genzel[1,2], Rebekka Grellmann[3], Maryam Habibi[1], Roberto Abuter[4], Matteo Accardo[4], António Amorim[5], Narsireddy Anugu[6], Gerardo Ávila[4], Myriam Benisty[7], Jean-Philippe Berger[7], Nicolas Blind[8], Henri Bonnet[4], Pierre Bourget[9], Wolfgang Brandner[10], Roland Brast[4], Alexander Buron[1], Alessio Caratti o Garatti[10,15], Frédéric Chapron[11], Yann Clénet[11], Claude Collin[11], Vincent Coudé du Foresto[11], Willem-Jan de Wit[9], Tim de Zeeuw[1,12], Casey Deen[1], Françoise Delplancke-Ströbele[4], Roderick Dembet[4], Frédéric Derie[4], Jason Dexter[1], Gilles Duvert[7], Monica Ebert[10], Andreas Eckart[3,13], Michael Esselborn[4], Pierre Fédou[11], Gert Finger[4], Paulo Garcia[6,9], Cesar Enrique Garcia Dabo[4], Rebeca Garcia Lopez[10,15], Feng Gao[1], Éric Gendron[11], Stefan Gillessen[1], Frédéric Gonté[4], Paulo Gordo[5], Ulrich Grözinger[10], Patricia Guajardo[9], Sylvain Guieu[7], Pierre Haguenauer[4], Oliver Hans[1], Xavier Haubois[9], Marcus Haug[1,4], Frank Haußmann[1], Thomas Henning[10], Stefan Hippler[10], Matthew Horrobin[3], Armin Huber[10], Zoltan Hubert[11], Norbert Hubin[4], Christian A. Hummel[4], Gerd Jakob[4], Lieselotte Jochum[4], Laurent Jocou[7], Andreas Kaufer[9], Stefan Kellner[1,13], Sarah Kendrew[10,14], Lothar Kern[4], Pierre Kervella[11], Mario Kiekebusch[4], Ralf Klein[10], Rainer Köhler[10,16], Johan Kolb[9], Martin Kulas[10], Sylvestre Lacour[11], Vincent Lapeyrère[11], Bernard Lazareff[7], Jean-Baptiste Le Bouquin[7], Pierre Léna[11], Rainer Lenzen[10], Samuel Lévêque[4], Chien-Cheng Lin[10], Magdalena Lippa[1], Yves Magnard[7], Leander Mehrgan[4], Antoine Mérand[4], Thibaut Moulin[7], Eric Müller[4], Friedrich Müller[10], Udo Neumann[10], Sylvain Oberti[4], Thomas Ott[1], Laurent Pallanca[9], Johana Panduro[10], Luca Pasquini[4], Thibaut Paumard[11], Isabelle Percheron[4], Karine Perraut[7], Guy Perrin[11], Andreas Pflüger[1], Thanh Phan Duc[4], Philipp M. Plewa[1], Dan Popovic[4], Sebastian Rabien[1], Andrés Ramírez[9], Jose Ramos[10], Christian Rau[1], Miguel Riquelme[9], Gustavo Rodríguez-Coira[11], Ralf-Rainer Rohloff[10], Alejandra Rosales[1], Gérard Rousset[11], Joel Sanchez-Bermudez[9,10], Silvia Scheithauer[10], Markus Schöller[4], Nicolas Schuhler[9], Jason Spyromilio[4], Odele Straub[11], Christian Straubmeier[3], Eckhard Sturm[1], Marcos Suarez[4], Konrad R.W. Tristram[9], Noel Ventura[7], Frédéric Vincent[11], Idel Waisberg[1], Imke Wank[3], Felix Widmann[1], Ekkehard Wieprecht[1], Michael Wiest[3], Erich Wiezorrek[1], Markus Wittkowski[4], Julien Woillez[4], Burkhard Wolff[4], Senol Yazici[1,3], Denis Ziegler[11], and Gérard Zins[9]

(Affiliations can be found after the references)

September 28, 2018

ABSTRACT

This work presents an interferometric study of the massive-binary fraction in the Orion Trapezium Cluster with the recently comissioned GRAVITY instrument. We observe a total of 16 stars of mainly OB spectral type. We find three previously unknown companions for θ^1 Ori B, θ^2 Ori B, and θ^2 Ori C. We determine a separation for the previously suspected companion of NU Ori. We confirm four companions for θ^1 Ori A, θ^1 Ori C, θ^1 Ori D, and θ^2 Ori A, all with substantially improved astrometry and photometric mass estimates. We refine the orbit of the eccentric high-mass binary θ^1 Ori C and we are able to derive a new orbit for θ^1 Ori D. We find a system mass of 21.7 $M_\odot$ and a period of 53 days. Together with other previously detected companions seen in spectroscopy or direct imaging, eleven of the 16 high-mass stars are multiple systems. We obtain a total number of 22 companions with separations up to 600 AU. The companion fraction of the early B and O stars in our sample is about 2, significantly higher than in earlier studies of mostly OB associations. The separation distribution hints towards a bimodality. Such a bimodality has been previously found in A stars, but rarely in OB binaries, which up to this point have been assumed to be mostly compact with a tail of wider companions. We also do not find a substantial population of equal-mass binaries. The observed distribution of mass ratios declines steeply with mass, and like the direct star counts, indicates that our companions follow a standard power law initial mass function. Again, this is in contrast to earlier findings of flat mass ratio distributions in OB associations. We exclude collision as a dominant formation mechanism but find no clear preference for core accretion or competitive accretion.

1. Introduction

Massive stars, defined as those with masses higher than 8 $M_\odot$, have an intense impact on the evolution of galaxies. The winds, UV radiation, massive outflows, and the heavy elements produced by high-mass stars influence the formation of stars and planets (see e.g. Bally et al. 2005) as well as the structure of galaxies (e.g. Kennicutt 1998). Despite their important role, the formation of massive stars is not well understood. High-mass stars have short lifetimes and spend a significant part of their life hidden within their parental dust and gas clouds. During this embedded phase, some fundamental evolutionary processes are difficult to observe. For a detailed review of high-mass star formation, see e.g. Shu et al. (1987); Zinnecker & Yorke (2007); Tan et al. (2014); Motte et al. (2018)

There are several indications that high-mass star formation is not just a scaled-up version of low-mass star formation. One indication is that massive stars tend to appear more often in multiple systems than lower mass stars (e.g. Chini et al. 2011; Sana et al. 2012). Zinnecker & Yorke (2007) found that the number of companions per star increases with stellar mass. For example, Duchêne & Kraus (2013) found 0.22 ± 0.06 companions for stars with masses $\lesssim 0.1$ $M_\odot$ and 1.3 ± 0.2 companions for primary stars with masses $\gtrsim 16$ $M_\odot$. They also found more multiple systems for stars with higher mass. At least 60% of stars with 8–16 $M_\odot$ are part of a multiple system. For stars $\gtrsim 16$ $M_\odot$, at least 80% are found in multiple systems (Duchêne & Kraus 2013; Sana et al. 2014). The higher number of companions and multiple systems is most likely a result of their formation process. Massive stars are short-lived and thus it is unlikely that they assemble all of their companions by random interactions in reasonable timescales. Duchêne & Kraus (2013) provides a review about stellar multiplicity. Moe & Di Stefano (2017) present a detailed study of the distribution and properties of early-type binaries.

In the case of massive star formation, two different scenarios try to explain the birth of a protostellar object from molecular gas. McKee & Tan (2002) proposed that molecular condensations in turbulent gas form a single massive protostar or several gravitationally bound protostars. For this "monolithic collapse", the mass of the final product is directly associated with the mass needed for star formation. Thus, the final material for the resulting star is already gathered before the beginning of star formation. Monolithic collapse or core accretion, assumes that the initial conditions are similar to low-mass star formation. An isolated core collapses and accretes mass with a disk (Yorke & Sonnhalter 2002). McKee & Tan (2002) proposed the turbulent core model, assuming mainly non-thermal internal pressure. Tan et al. (2014) pointed out that the accretion rate of the turbulent core model is higher than for competitive accretion. In the past it was believed that radiation pressure of young massive stars could halt accretion (see e.g. Zinnecker & Yorke 2007; Krumholz 2015). This has been solved by introducing non-spherical accretion (see e.g. Krumholz et al. 2009).

Bonnell et al. (1997, 2001) described an alternative scenario in which the core or resulting protostar moves within the cloud, independent of the movement of the surrounding gas. Thus, the material can come from different parts of the parent cloud, as well as from material infalling onto the cloud. Each of the forming protostars competes for the material; this mechanism is therefore called "competitive accretion". Competitive accretion starts with many low-mass seeds in a parent cloud, which start to accrete mass, e.g. Krumholz (2016, pp. 213). Two factors influence the amount of growth for stars with competitive accretion (see e.g. Bonnell et al. 1997, 2001). One is the accretion radius or the accretion domain, meaning the range where gas is gravitationally attracted to the star. The second factor is the gas density of the accretion domain. Because gas flows down to the center of clusters, the central position in a cluster is beneficial for mass growth. When the accretion volumes start to overlap, the stars are competing for the available material. This might explains why massive stars are rare and mainly form in the most favorable, i.e. densest, conditions. However, there are also a few examples of O-type stars born in isolation (de Wit, W. J. et al. 2004, 2005; Oskinova et al. 2013).

The accretion rate for competitive accretion is lower than for monolithic collapse (see e.g. Tan et al. 2014; Krumholz 2016). The angular momentum of gas in both cases is large enough to form an accretion disk.

Companion stars can be formed by various mechanisms. In the monolithic collapse scenario, a massive core can fragment into several smaller cores and form a binary or multiple system (see e.g. Krumholz 2016; Tan et al. 2014, and references therein). Disk fragmentation can also produce companion stars, see e.g. Kratter & Lodato (2016). They concluded that for a star with 8 $M_{\odot}$, the disk cools down sufficiently to undergo disk fragmentation for separations ≥ 50 astronomical units (AU). Krumholz (2016, p. 296) stated that the typical accretion rates on a stellar core lead to a high surface density of the disk and eventually result in disk fragmentation.

Another possible scenario for the formation of companions is the failed merging of two stars. This process requires a high stellar density, which is much higher than the typical observed density in our Galaxy. Zinnecker & Yorke (2007) concluded that the cross section is small and that the collision impact parameter requires fine tuning. If there is a disk, the capture of a companion star becomes more likely.

Additionally, a binary system can capture a third, massive companion — a mechanism called "three body capture". In a simulation of a protostellar cluster with more than 400 stars, Bonnell et al. (2003) demonstrated that dynamical three-body capture is common in protoclusters.

In order to gain a deeper understanding of massive star and cluster formation, the characteristics of binaries need to be determined. Lada & Lada (2003); Briceño et al. (2007) found that massive star formation results in either dense OB clusters or unbound OB associations. The Orion Nebula Cluster, at a distance of 414 pc (Menten et al. 2007; Reid et al. 2014), is one of the closest active star-forming regions. For a general overview see e.g. Genzel & Stutzki (1989); Hillenbrand (1997); Muench et al. (2008). The Orion Nebula Cluster comprises an expanding blister HII region with the Orion Trapezium Cluster (θ^1), an open cluster of young massive stars, at its center. These centrally concentrated young stars cause the ionization of the surrounding cloud. The Orion Trapezium Cluster has six principal components, θ^1 Ori A to θ^1 Ori F. The stars θ^1 Ori (A, B, C, D) are all known to have companions.

The Orion Nebula Cluster has already been thoroughly observed in recent decades. Deep spectroscopic surveys probed for close companions on scales $\lesssim$ 1 AU (e.g. Morrell & Levato 1991; Abt et al. 1991). Adaptive optic assisted imaging and speckle interferometry resolved companions $\gtrsim$ 14–few 100 AU (e.g. Weigelt et al. 1999; Preibisch et al. 1999; Schertl et al. 2003). While these ranges have been covered, there is still a gap in the separations where observations are scarce. The region $\sim$1–few 10 AU can only be resolved with long baseline interferometry.

In the following, we present the observational data obtained with GRAVITY (Gravity Collaboration et al. 2017), a K-band interferometric instrument at the Very Large Telescope Interferometer (VLTI). In Section 2, we describe our observations. Section 3 introduces the data analysis. We present our results in Section 4, discuss the results in Section 5, and conclude in Section 6.

2. Observations

Data were taken with GRAVITY, a novel instrument at the VLTI for $\sim$10 micro-arcsecond astrometric precision measurements with K-band interferometry (Gravity Collaboration et al. 2017). GRAVITY coherently combines the light of all four UTs (8.2 m diameter) or all four ATs (1.8 m diameter) with two interferometric beam combiners for fringe tracking and observing science objects, respectively. A star up to 10 mag in K-band can be used for fringe-tracking faint objects up to 17 mag in the science channel using the UTs. The spectrometers provide three spectral resolutions: low, medium, and high, with $R \sim 22, 500, 4000$, respectively.

Table 1 provides an overview of all observations. The 16 brightest objects in the Orion Nebula were selected for this study. Observations were primarily performed in medium resolution with the astrometric configuration of the ATs at the stations A0-G1-J2-K0. The detector integration time – DIT – depends on the source luminosity. A higher DIT is needed for fainter objects (e.g. a DIT of 30 s was used for θ^1 Ori F with a K-magnitude of 8.38) whereas shorter DITs are possible for bright objects (e.g. 3 s or 5 s for θ^1 Ori C with a K-magnitude of 4.57). The integration on the source is repeated several times, usually followed by a sky background observation with the same DIT and number of repetitions (NDIT). Data were reduced with the standard GRAVITY pipeline (Gravity Collaboration et al. 2017). The reduction algorithm follows the approach of Tatulli et al. (2007) and creates a Pixel to Visibility Matrix (P2VM). The visibility is measured by combining the telescope beams with a relative phase shift of $0°, 90°, 180°$, and $270°$. Thus, we get four signals per baseline, resulting in $4 \cdot 6 = 24$ channels for the science object (Gravity Collaboration et al. 2017). The P2VM provides the phase relations, photometry, and coherence of the four incoming telescope beams and the 24 outgoing signals. A detailed description of the reduction is provided in Lapeyrere et al. (2014) and an additional example of the use of

GRAVITY to the study of massive multiple systems can be found in Sanchez-Bermudez et al. (2017).

For the instrument calibration, we also need to calibrate the wavelength of the fringe tracker and science channel, as well as to determine the dark field, bad pixels, and to compute the profile of the spectra with a flat field. Using the P2VM, we then compute real-time visibilities. Each file has several frames, one for each integration. The frames are averaged during reduction.

For the calibration of the visibilities we observe point-like objects with a known diameter and which can be considered single stars. As we know the true shapes of the calibrator visibilities, we compute a visibility transfer function to adjust the measured visibilities to match the expected visibilities. This visibility transfer function is then applied to the visibilities of the science object.

3. Data Analysis

In this section, we provide an overview of the modeling functions and tools used for data analysis. In the beginning, the observed data is fitted according to a binary model. For sufficiently well-sampled data, we are able to determine the orbital parameters of the binaries. In order to accurately determine the companion magnitude, we need to consider the effects of dust extinction. Finally, we provide a detection limit for our observations.

3.1. Modeling a Binary Star

We introduce the modeling functions that were used for analyzing the data. We assume a binary model and use it to fit the squared visibilities, closure phase and triple amplitude of our observational data.

Visibility Visibility of a binary model is described as:

$$\nu_{\mathrm{bin}} = \frac{\nu_{\mathrm{main}} + f \cdot \nu_{\mathrm{comp}} \exp\left(-2i\pi \dfrac{u \cdot \Delta\alpha + v \cdot \Delta\delta}{\lambda}\right)}{(1 + f)}, \tag{1}$$

where ν_{main} and ν_{comp} are the complex visibilities for the primary and the companion star, respectively (see, for example, Lawson (2000)). In the case of an unresolved star, $\nu_{\mathrm{main}} = \nu_{\mathrm{comp}} = 1$. The parameters u and v are the spatial frequencies of the telescope baselines; λ is the observed wavelength; $\Delta\alpha$ and $\Delta\delta$ are the angular distances of the companion star from the primary star in R.A. and Dec., respectively; and $f = f_{\mathrm{comp}}/f_{\mathrm{main}}$ is the mean flux ratio over all wavelengths of the system, where f_{comp} and f_{main} are the flux of the companion star and primary star, respectively.

The parameters u, v, and λ are provided by the observational data, while the distances $\Delta\alpha$ and $\Delta\delta$ together with the flux ratio f are variable parameters to be fitted. To find starting values for these parameters, we use a grid-search algorithm. We scan $\Delta\alpha$ and $\Delta\delta$ between either ± 200 mas, ± 100 mas or ± 50 mas in steps of either 1 or 0.5 mas, and the flux ratio f between 0 and 1 in steps of 0.1. The best result of the grid-search forms the starting values for the subsequent weighted least-squares optimization, using the Levenberg-Marquardt algorithm and the LMFIT package (Newville et al. 2014).

Closure phase and triple amplitude The closure phase (CP) is computed by taking the argument of the bispectrum of the visibility function. The bispectrum is the triple product

of complex visibilites for the telescopes i, j, k:

$$CP(i, j, k) = \arg\left(\nu_{\mathrm{bin,ij}}\nu_{\mathrm{bin,jk}}\nu_{\mathrm{bin,ki}}\right) \tag{2}$$

where the complex visibilites ν_{bin} are computed using Equation (1).

The triple amplitude is the modulus of the bispectrum. Most of the information is contained in the closure phase, thus, the triple amplitude is not always necessary for fitting the data. The optimization is done in the same way as for the visibility model.

3.2. Orbit Modeling

For fitting the orbit, we use the KeplerEllipse class of PyAstronomy[1] to determine the position at a given time for a set of orbital elements. This position is then compared with the positions obtained from the binary model fit (see Section 3.1). The optimization is done with the Trust-region method, which supports boundaries of variables in contrast to a regular least-squares minimization.

The parameters of the orbit are defined as follows: a is the semi-major axis of the Kepler ellipse, P is the orbital period, e the eccentricity, τ the time of periapsis passage, Ω the longitude of the ascending node, ω the argument of periastron, and i the inclination of the orbit. The ascending node is defined as the point where the orbiting object passes the plane of reference in the direction of the observer. All parameters are in units of the respective initial guess. The semi-major axis a is thus mostly reported in units of angular separation. For a more detailed discussion see e.g. Roy (2005, pp. 22-24).

As an observer, we see the 3D-orbit projected on a 2D-plane. The projection of different orbits can appear similar on the plane of reference, e.g. a highly inclined and eccentric orbit can appear as a not inclined circular orbit.

In order to not get stuck in a local minimum of χ^2, a good starting value is essential for optimization. If orbital elements are already determined in the literature, we take these elements as starting values for the optimization, e.g the values from Kraus et al. (2009) for the orbit of θ^1 Ori C_2 (see Section 4.1.3). If there are no previously determined orbital elements, we use the Basin-Hopping algorithm (Wales & Doye 1997), to find a global minimum and use the result as starting value for the Trust-region method.

3.3. Dust Extinction

For calculating the luminosity or absolute magnitude of a star, we need to consider its spectral type and extinction effects of the interstellar and circumstellar medium. $A(\lambda)$ is the extinction at wavelength λ in magnitudes. The extinction of color is described by e.g. $E(B-V) = A(B) - A(V)$, with B as the filter for $\sim440 \pm 90$ nm and V as the filter for $\sim545 \pm 84$ nm. The interstellar reddening law is $R_V = A(V)/E(B-V)$. For the diffuse interstellar medium, a typical value is $R_V = 3.1$, whereas for dense clouds the value is $R_V = 5$ (Allen & Cox 2000, p. 527). In the K-band and for $R_V = 3.1$, we get $A(K) = 0.108A(V)$.

3.4. Photometric Mass

To get a mass estimate based on the magnitude, we use the isochrones in Allen & Cox (2000, p. 151, p. 388, and references therein) and Salaris & Cassisi (2005, p. 130). With the first and second table, we get M_K for different spectral types and temperatures. With the effective temperatures in both tables, we link M_K to stellar masses using the third table.
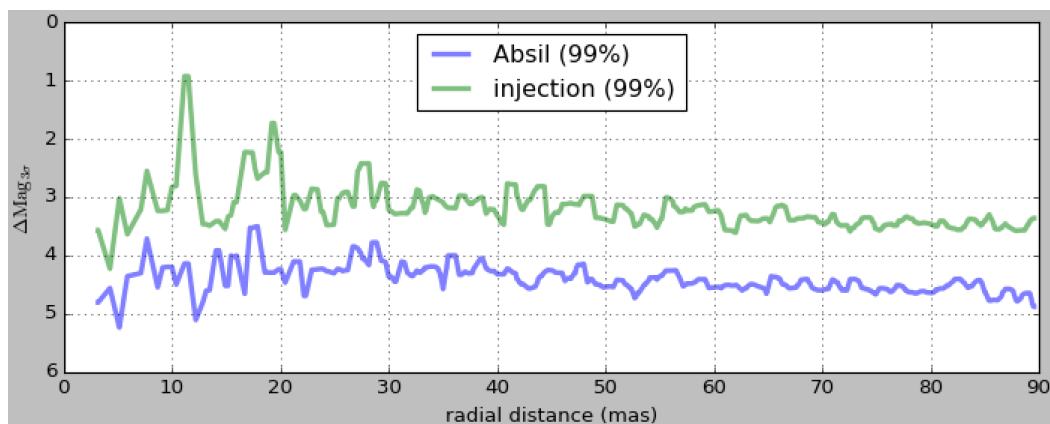
---

[1] https://github.com/sczesla/PyAstronomy

Fig. 1. Example for the companion detection limit for θ^1 Ori B, observed at the 12th October 2017, as determined with CANDID. The detection limit on the y-axis is denoted as a magnitude difference to the main star. The x-axis shows the separation in mas.

Now we can compare the values for M_K from the table to $M_K(Star)$ and get an estimate of mass and spectral type. The tables are for class V stars, meaning hydrogen-burning main sequence stars. For pre-main sequence (PMS) stars, the values are not accurate, merely representing a rough estimation.

3.5. Companion Detection Limits

We use CANDID (Gallenne et al. 2015) for determining detection limits of companion stars. CANDID is a Python tool which looks for high contrast companions. It provides two methods for computing limits.

The first method follows the approach of Absil et al. (2011). Absil et al. (2011) inserted a binary model at different positions (α, β). They then compared the probability of the binary model with the probability of a uniform disk model, assuming the uniform disk is the true model.

The second approach changes the null hypothesis. They injected companions at different positions with different flux ratios. Then, they determined the probability of the binary model being the true model, compared with the model of a uniform disk. In other words, the first approach tries to reconstruct a uniform disk model from binary data. The second approach tries to reconstruct a binary model from binary data. The second method yields more conservative results, which is why we choose it to determine our detection limits. Figure 1 shows an example of the companion detection limit for θ^1 Ori C. We take the worst limit as our companion detection limit.

4. The Orion Nebula Cluster M42

One of the closest active star forming regions is the Orion Nebula Cluster (ONC), at a distance of 414 ± 7 (Menten et al. 2007; Reid et al. 2014). The ONC is located in a giant molecular cloud, at the sword of Orion. A young star cluster (younger than 1 Myr) is located in the center of the Nebula – see e.g. Muench et al. (2008). This central region is called the "Orion Trapezium Cluster" (OTC) or θ^1 Orionis. The OTC is dominated by θ^1 Ori C, a young O-star with $\sim 34\ M_\odot$. The radiation and outflow of θ^1 Ori C caused the ionization of its vicinity. The H II region expanded into the surrounding molecular cloud and dissolved the molecular gas in which the young stars had been born. This process exposed large parts of the embedded star clusters and created the ONC.

4.1. Orion Trapezium Cluster Stars

In this study, we concentrate on the most luminous stars of the ONC. In the Trapezium Cluster, we observe stars with apparent K-magnitudes ranging from 4.57 to 8.38. In the following, we summarize previous results and present our findings for each of the observed targets.

4.1.1. θ^1 Ori A (HD 37020, Brun 587, TCC 45, Parenago 1865)

θ^1 Ori A_1 is a B0.5-type star (Levato & Abt 1976; Simón-Díaz et al. 2006) with a K-band magnitude $m_K = 5.67$ (Cutri et al. 2003). Hillenbrand (1997) found a mass of 18.91 $M_\odot$ and an extinction of $A_V = 1.89$ mag. Weigelt et al. (1999) calculated a mass of 20 $M_\odot$ and Schertl et al. (2003) assumed a mass of 16 $M_\odot$, whereas Simón-Díaz et al. (2006) found a mass of 14 ± 5 $M_\odot$ and a radius of $6.3 \pm 0.9 R_\odot$.

Lohsen (1975) found an eclipsing binary with a period of 65.43 days (Mattei & Baldwin 1976), which we will refer to as A_3. Abt et al. (1991) derived a period of 65.09 ± 0.07 days from their measured radial velocities for θ^1 Ori A_3. Bossi et al. (1989) concluded that the thermal spectrum and features correspond to a T Tauri companion with a mass between 2.5 and 2.7 $M_\odot$ at a separation of 0.71 AU. However, Vitrichenko & Plachinda (2001) determined a greater distance of 0.93 ± 0.07 AU.

Petr et al. (1998) discovered a third companion (A_2) at a separation of $\sim$200 mas, which corresponds to a projected distance of $\sim$90–100 AU (see e.g. Weigelt et al. 1999; Preibisch et al. 1999; Close et al. 2012). Schertl et al. (2003) determined a mass of 4 $M_\odot$ for θ^1 Ori A_2 and suggested a period of $P \sim 214$ yr. θ^1 Ori A_2 is an F-type star extincted by $A_V \sim 3.8$ mag (Schertl et al. 2003).

Until now, it has not been entirely clear whether A_2 is gravitationally bound to θ^1 Ori $A_{1,3}$. We used GRAVITY data taken between November 2015 and January 2018 (Table 1) to get precise separation vectors. Our position measurements show an acceleration towards the primary star, proving that the system is gravitationally bound. In Figure 2 one can see a motion of the companion star towards the main object. We use only the position measurements, because the spectral resolution is too low for precise radial velocity measurements. From the measured flux ratio $f \sim 0.23 \pm 0.05$ we infer a magnitude of $m_K = 7.3 \pm 0.3$.

4.1.2. θ^1 Ori B (HD 37021, Brun 595, TCC 56, TCC 60, Parenago 1863)

θ^1 Ori B consists of at least six hierarchical components. θ^1 Ori B_1 is a B1V-type star (Mason et al. 1998) with a magnitude $m_K = 6.00$ (Cutri et al. 2003). Hillenbrand (1997) determined a mass of 7.18 $M_\odot$ for an extinction of $A_V = 0.49$. Weigelt et al. (1999) estimated a consistent mass of $m = 7$ $M_\odot$.

Petr et al. (1998) found a visual companion at a separation of approximately $1''$, corresponding to 415 AU projected distance (Close et al. 2012) at 450 pc. Taking the 414 ± 7 pc from Menten et al. (2007); Reid et al. (2014), the projected separation becomes 382 ± 6 AU. This companion itself is a resolved binary (θ^1 Ori $B_{2,3}$, see Figure 3) with 49 ± 1 AU projected separation and a period of $\sim$200 yr (Close et al. 2013). Their K-magnitudes are estimated to be 7.6 and 8.6 (Close et al. 2012). According to Close et al. (2013), $B_{2,3}$ has a system mass of $\sim$5.5 $M_\odot$, which is in the same order of magnitude as the masses determined by Schertl et al. (2003) with $m_{B_2} = 4$ $M_\odot$, and $m_{B_3} = 3$ $M_\odot$. However, it differs from the values found by Preibisch et al. (1999), which are $m_{B_2} = 1.6$ $M_\odot$, and $m_{B_3} = 0.7$ $M_\odot$. The inferred orbital period of $B_{2,3}$ around the main star depends on the
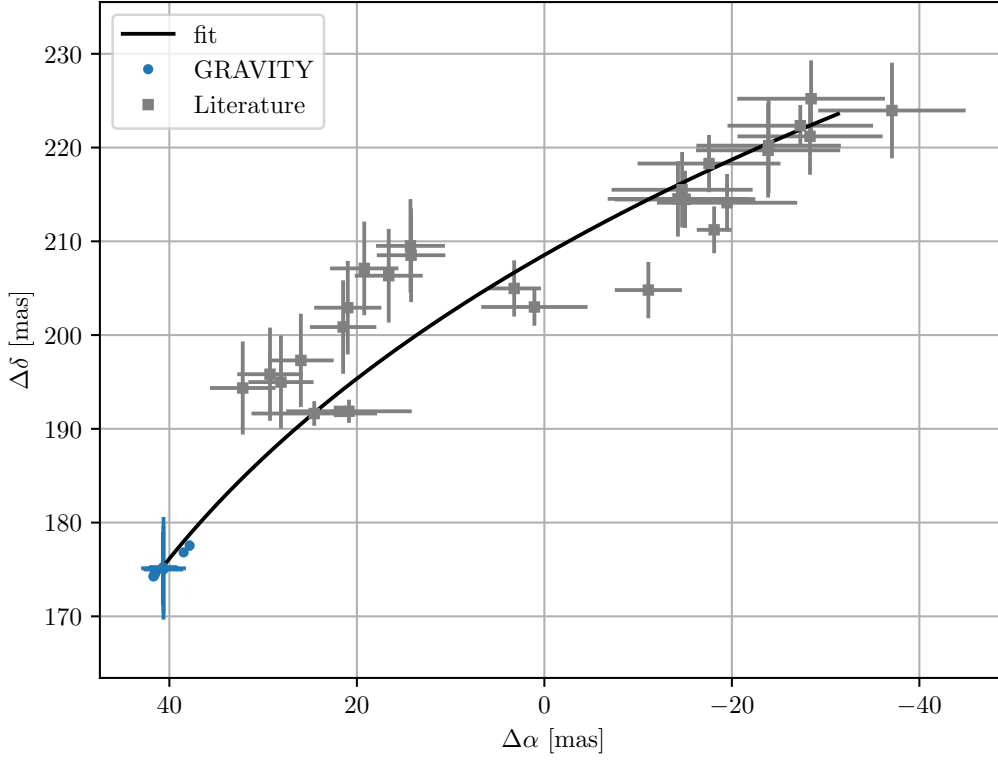
Fig. 2. Measured positions of θ^1 Ori A_2, with east to the left. The primary star θ^1 Ori A_1 is located at position (0,0). Blue dotted positions were observed with GRAVITY. For some of the dots, the errorbar is smaller than the symbol displayed. Grey/square positions are taken from Close et al. (2012), Schertl et al. (2003), Petr et al. (1998), Weigelt et al. (1999), Balega et al. (2004), Balega et al. (2007), and Grellmann et al. (2013).
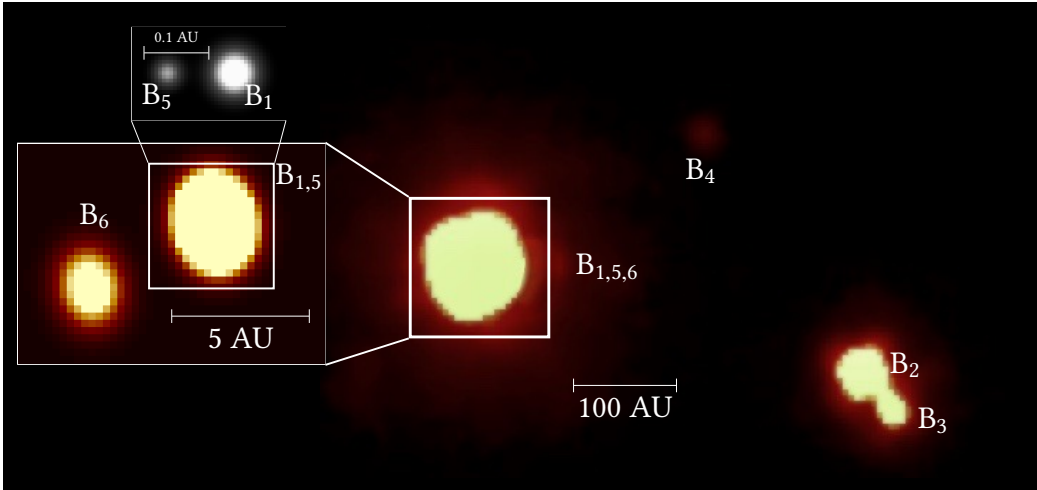

Fig. 3. Main image: θ^1 Ori B group imaged in H-band. B_1 is an eclipsing binary $B_{1,5}$. It was created with NaCo data, based on data obtained from the ESO Science Archive Facility under request number 342335, ESO programme 60.A-9800(J). Additionally, with GRAVITY we detected another companion B_6 at a separation of ~13 mas, shown in the zoomed image of $B_{1,5,6}$ (K-band). The image of B_6 orbiting $B_{1,5}$ is reconstructed from our observations. The zoom into the spectroscopic binary $B_{1,5}$ is only a representative image and was not created with observational data.

inclination of the orbit. For a less inclined orbit, Close et al. (2012) determined a period of $P \sim 1920$ yr, whereas in Close et al. (2013) a highly inclined orbit was assumed and resulted in a period of $P \sim 11\,000$ yr with an absolute separation of ~820 ± 14 AU.

Located $0.6''$ $\sim 248 \pm 4$ AU north-west of B_1 is another faint companion (Figure 3), θ^1 Ori B_4 (Simon et al. 1999) with $m_K = 11.66$ (Close et al. 2012). Close et al. (2013) determined a period of $\sim 2000 \pm 700$ yr. Preibisch et al. (1999) estimated the mass of B4 to be $m_{B_4} = 0.2~M_\odot$ and sets an upper mass limit of $< 2~M_\odot$. In contrast, we estimate the mass of B_4 to be $m_{B_4} \sim 1~M_\odot$, which is consistent with the limit of Preibisch et al. (1999).

Considering an extinction of $A_V = 0.49$ (Hillenbrand 1997), we calculate an absolute magnitude $M_K(B_4) = 3.57$ and compare the magnitude with the isochrones. This yields the mass estimate of $1~M_\odot$. Because of its low mass, B_4 may be ejected from the system at a certain point, but appears temporarily stable (Close et al. 2013).

Hartwig (1921) and Schneller (1948) found θ^1 Ori B_1 to be an eclipsing binary (θ^1 Ori $B_{1,5}$) with a 6.47 day period (Abt et al. 1991). Popper & Plavec (1976) determined θ^1 Ori B_5 to be a late A-type star and a mass ratio of $q = m_{B_5}/m_{B_1} \sim 0.3$, which leads to $m_{B_5} \sim 2~M_\odot$. On the other hand, Close et al. (2003, 2012, 2013) assumed a mass of $7~M_\odot$ for B_5, but did not justify their assumption. Close et al. (2012) determined a separation of 0.13 AU assuming a distance to the OTC of 450 pc. With the distance of 414 ± 7 pc determined by Menten et al. (2007); Reid et al. (2014), this converts to a separation of 0.120 ± 0.002 AU.

Vitrichenko et al. (2006) claim the detection of a late type companion based on radial velocity anomalies. Further observations are needed to verify the detection.

With GRAVITY, we detect a previously unknown companion B_6 at separations between 8.5–17.2 mas, corresponding to a projected distance between 3.52 ± 0.05 AU and 7.12 ± 0.12 AU. The average flux ratio is 0.31 ± 0.06 and corresponds to an apparent K-magnitude of $m_{B_6} = 7.3 \pm 0.5$. Considering the absorption, the absolute K-magnitude is $M_K(B_6) = -0.84 \pm 0.6$. The comparison with isochrones from Allen & Cox (2000, p. 150, p. 388) and Salaris & Cassisi (2005, p. 130) yields a mass $m_{B_6} \sim 4$–$6~M_\odot$, which corresponds to a B-type star. Vasileiskii & Vitrichenko (2000) suggested a close B-type companion to explain a secondary minimum observed in the eclipse of B_1. This supports our spectral classification of B_6.

θ^1 Ori B_6 was observed between January 2017 and January 2018 (see Table 1). The position of the star relative to θ^1 Ori $B_{1,5}$ is presented in Figure 4 and shows orbital motion. For the determination of orbital parameters further observations are needed. We approximate the orbital path by fitting values for $\Delta\alpha$ and $\Delta\delta$ over time with a quadratic function. The resulting path is the black line in Figure 4. The residuals to this fit scatter by a root mean square (RMS) of 0.05 mas in δ and 0.06 mas in α as can be seen in Figure 5.

With CANDID (Gallenne et al. 2015, see Section 3.5), we can exclude further companions at a 3σ level with $\Delta m < 3.5$, thus a mass $> 1.9~M_\odot$ for separations of 1.7–8.3 AU. For the range of 8.3–16.6 AU, the limit is 5 mag ($\approx 1.5~M_\odot$) and for 16.6–46.8 AU, we can exclude companions with $\Delta m = 5.2$ ($\approx 1.1~M_\odot$).

4.1.3. θ^1 Ori C (HD 37022, Brun 598, TCC 68, Parenago 1891)

θ^1 Ori C_1 is a O7V-type star (Sota et al. 2011) and the brightest and most massive member of the Trapezium Cluster with $m_K = 4.57$ (Ducati 2002). Furthermore, it is one out of few O-stars with detected magnetic fields (Stahl et al. 1996; Donati et al. 2002; Grunhut et al. 2017). Stahl et al. (1993) discovered variations in the spectrum with a 15.43 day period. This variation also appears in X-ray, radial velocities, and magnetic fields, discussed by, for example, Stahl et al. (2008), Wade et al. (2006), Simón-Díaz et al. (2006), and references therein. The magnetic field direction does not match the spin axis, which is an indication that θ^1 Ori C_1 was formed in a collision process (Zinnecker & Yorke 2007).
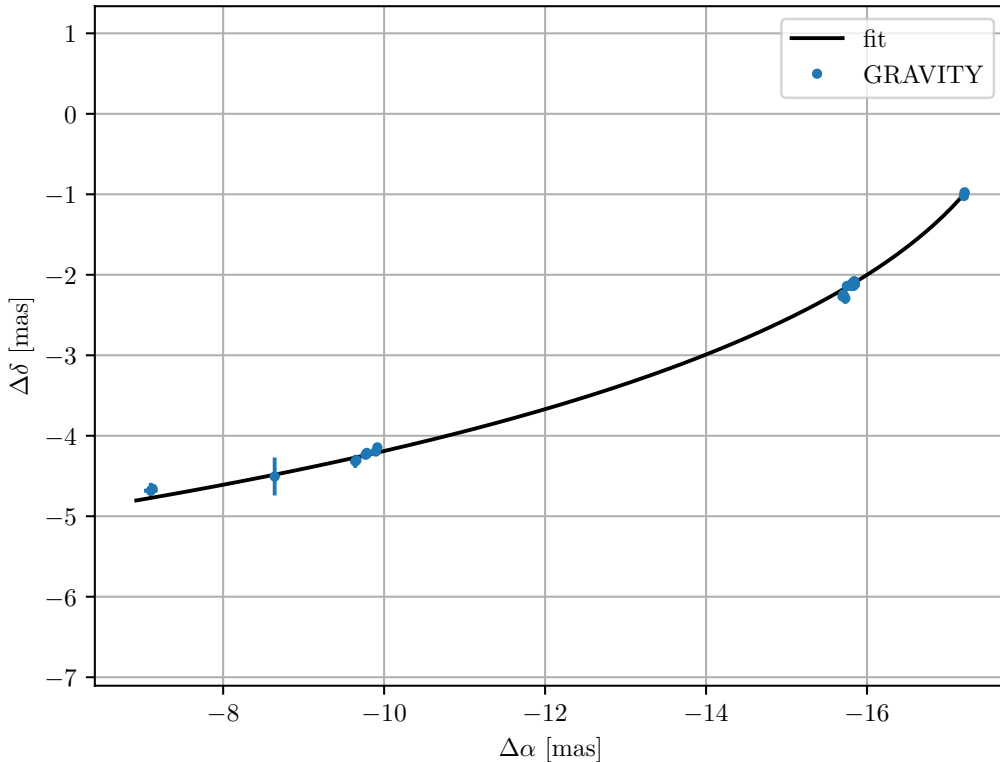
Fig. 4. Positions of B_6 between January 2017 and January 2018. We see orbital motion around $B_{1,5}$ at (0,0), moving from east (left) to west (right).
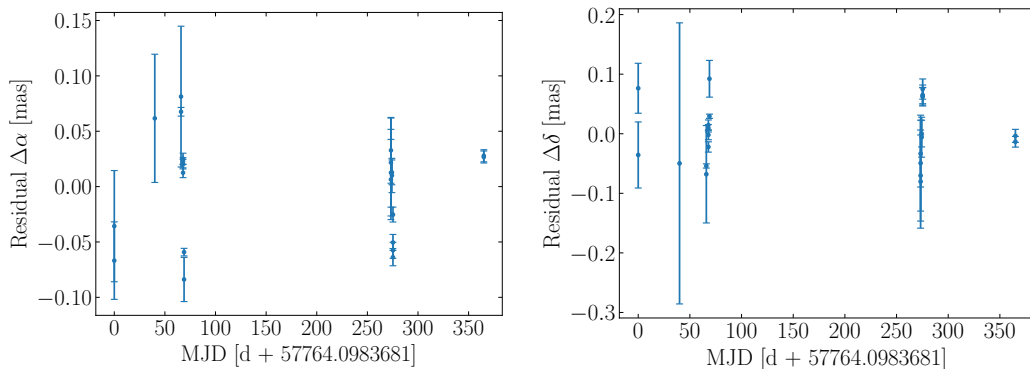

Fig. 5. Residuals of the $\Delta\alpha$ (left) and $\Delta\delta$ (right) positions from the best fit. The RMS is 0.05 mas in δ and 0.06 mas in α.

Weigelt et al. (1999) discovered a close visual companion C_2 at a separation of 33 mas. Kraus et al. (2009) determined the orbital parameters in Table 2 and a resulting mass ratio of $q(414\mathrm{pc}) = m_{C_2}/m_{C_1} = 0.23 \pm 0.05$. They estimate a total system mass of $44 \pm 7\ M_\odot$ and a dynamical distance of 410 ± 20 pc.

Using the calibration models from Martins et al. (2005), Kraus et al. (2007) derived a mass of $m_{C_1} = 34\ M_\odot$, an effective temperature $T_{\mathrm{eff},C_1} = 39\,900$ K, and $\log L_{C_1}/L_\odot = 5.41$. The resulting parameters for the companion star are $m_{C_2} = 15.5\ M_\odot$, $T_{\mathrm{eff},C_2} = 31900$ K and $\log L_{C_2}/L_\odot = 4.68$, thus implying a O9.5-type star. The temperatures are in accordance with Simón-Díaz et al. (2006), who found temperatures of $T_{\mathrm{eff},C_1} = 39\,000 \pm 1000$ K and derived a stellar radius of $R_{C_1} = 10.6 \pm 1.5\ R_\odot$. The spectroscopic mass of $45\ M_\odot$ and evolutionary mass of $33\ M_\odot$ for θ^1 Ori C_1 by Simón-Díaz et al. (2006) differ. Herrero et al. (1992) described a discrepancy between spectroscopic masses and masses determined using

	Kraus et al. (2009)	Balega et al. (2015)	This work
a [mas]	43.61 ± 3	45 ± 3	45 ± 2
P [yr]	11.26 ± 0.5	11.28 ± 0.02	11.4 ± 0.2
e	0.592 ± 0.07	0.59 ± 0.01	0.59 ± 0.04
τ	2002.57 ± 0.5	2002.59 ± 0.02	2002.2 ± 0.2
Ω [°]	26.5 ± 1.7	28.3 ± 0.3	27.9 ± 0.7
ω [°]	285.8 ± 8.5	286.1 ± 0.2	283 ± 2
i [°]	99.0 ± 2.6	98.9 ± 0.4	98.6 ± 0.6

Table 2. Orbital parameter for θ^1 Ori C determined by Kraus et al. (2009), Balega et al. (2015) and in this work including GRAVITY data. a is the semi-major axis in mas (44 mas = 18.2 ± 0.3 AU), P the period in years, e the eccentricity, τ the time of the periastron passage, Ω the longitude of the ascending node, ω the argument of periapsis, and i the inclination of the orbit. The results of Kraus et al. (2009) and this work agree within the error bars. The results of Balega et al. (2015) differ in τ and ω with this work.

an evolutionary model. Habibi et al. (2017) pointed out that spectroscopic masses are sensitive to $\log g$ and that an error of 0.1 (as in Simón-Díaz et al. 2006) in $\log g$ translates to a factor of $10^{0.1} \approx 1.26$, or an uncertainty of 126% for spectroscopic masses. Balega et al. (2015) added spectroscopic observations to the previous data and determined a total system mass of 45.5 ± 10 $M_\odot$, a mass ratio of $q = 0.36 \pm 0.05$ and derived $m_{C_1} = 33.5 \pm 5.2$ $M_\odot$ and $m_{C_2} = 12 \pm 3$ $M_\odot$. The separation of 44 ± 3 mas corresponds to 18.2 ± 1.2 AU.

GRAVITY observations from November 2015 to January 2018 (for a list of observations see Table 1) show a variation of the flux ratio $f = f_{C_2}/f_{C_1}$ between 0.18 and 0.36, which points to a non-constant brightness of either the primary or the companion star or both stars. We compute an average K-magnitude of 6.0 ± 0.4. The extinction is $A_V = 1.74$ (Hillenbrand 1997) and using the method described in the previous section, we infer a spectral type of B1 or younger and thus a stellar mass > 10 $M_\odot$ (Allen & Cox 2000, p. 389). Looking at the flux ratio f depending on wavelength (Figure 6), we notice a drop at 2166 nm — the Br-γ line. This points to an absorption of C_2 in the Br-γ line. For the given example in Figure 6, C_2 is 1.3 times fainter at the Br-γ line than at other wavelengths. With the new GRAVITY data, we fit the orbit of C_2 (see Figure 7) and find that our results agree with the parameters from Kraus et al. (2009). Table 2 presents both outcomes, and the orbital elements determined by Balega et al. (2015).

Vitrichenko (2002b) and Lehmann et al. (2010) found another spectroscopic companion C_3 with a period of 61.5 days, resulting in an estimated separation of ~ 1 mas. They derived masses of 31 $M_\odot$ for C_1, 12 $M_\odot$ for C_2, and 1.0 ± 0.2 $M_\odot$ for C_3. For a primary star with 33 $M_\odot$ and a companion star with 1 $M_\odot$, we expect a reflex motion of ~ 60 μas for C_1. To this point, we have not detected such wobbling, probably because the position scattering was too large. The residuals from the orbit are shown in Figure 8. The RMS of the residuals is 0.07 mas for $\Delta\alpha$ and 0.05 mas for $\Delta\delta$.

With CANDID, we set a limit on further companions at a 3σ level. For separations of 1.70–8.3 AU, we compute $\Delta m < 3.2$ (≈ 3 $M_\odot$). For the range of 8.3–46.8 AU, we can exclude companions with $\Delta m < 4.2$ (≈ 2.2 $M_\odot$).

4.1.4. θ^1 Ori D (HD 37023, Brun 612, Parenago 1889)

θ^1 Ori D is a pre-main sequence B1.5V-type star (Levenhagen & Leister 2006) with a K-magnitude of 5.75 (Cutri et al. 2003). Hillenbrand (1997) found a mass of 16.6 $M_\odot$, whereas Simón-Díaz et al. (2006) derived a mass of 18 ± 6 $M_\odot$. Levenhagen & Leister (2006) found a mass of 11 ± 1 $M_\odot$ and Voss et al. (2010) determined a mass of 17.7 $M_\odot$ using rotating stellar models.
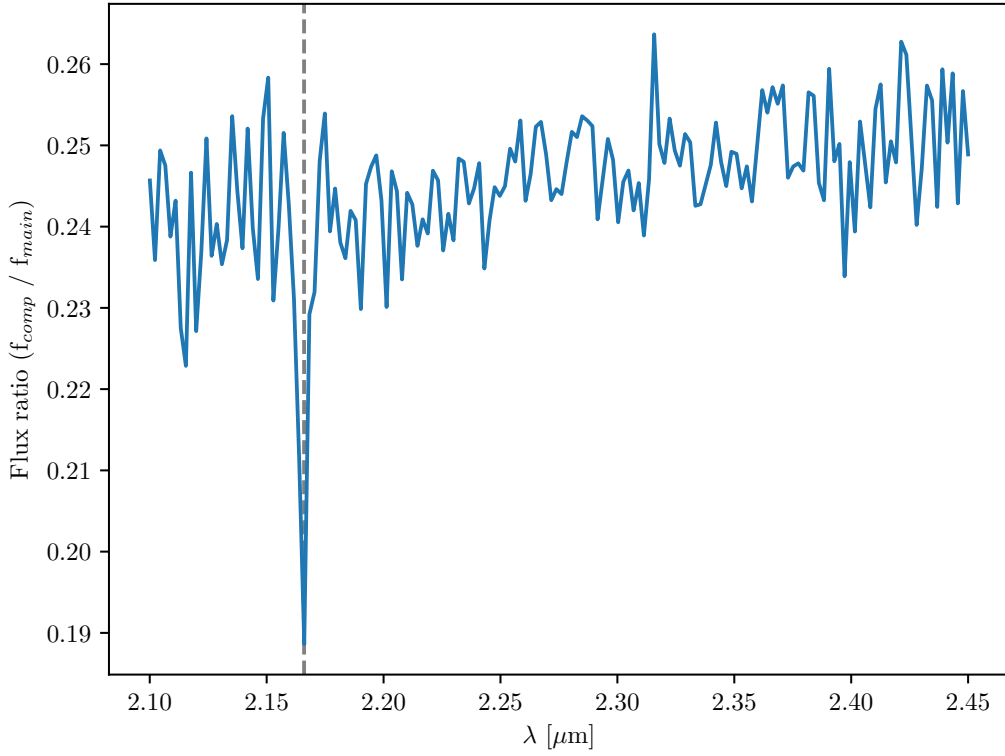
Fig. 6. Flux ratio $f = f_{C_2}/f_{C_1}$ as a function of observed wavelength. The vertical dashed grey line is at 2.166 microns, the Br-γ line. The drop indicates that C_1 has a much higher flux at that wavelength than C_2. Data were observed at January 9th 2016.
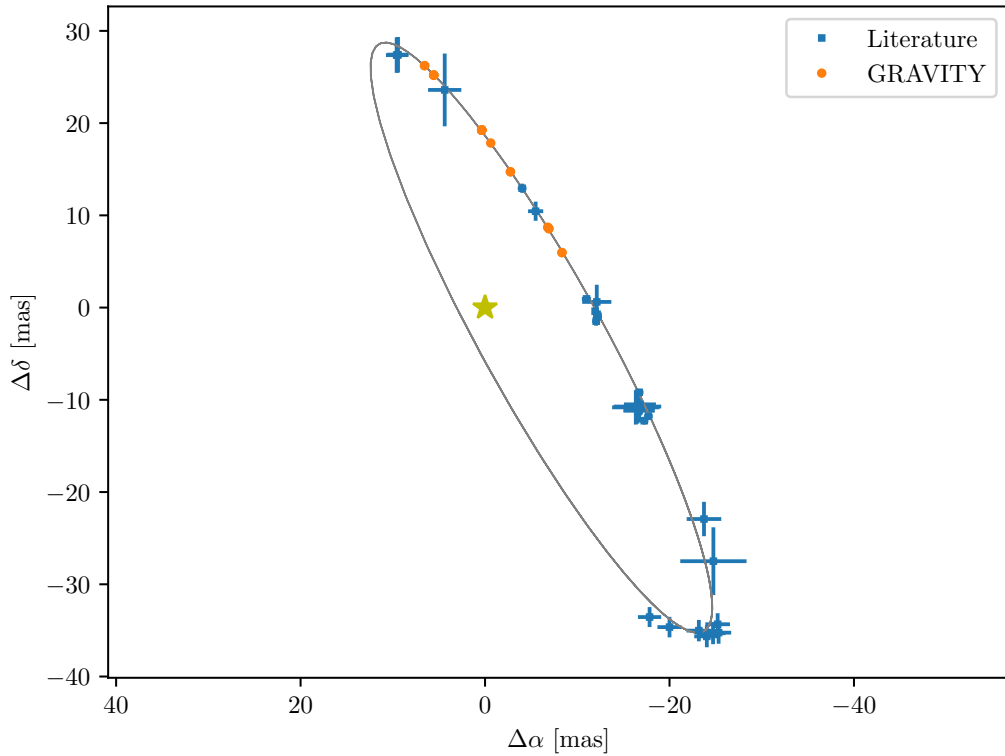

Fig. 7. Orbit of θ^1 Ori C_2. Orange dots are observed with GRAVITY, blue squares are positions taken from Weigelt et al. (1999), Schertl et al. (2003), Kraus et al. (2007), Patience et al. (2008), Kraus et al. (2009), and Grellmann et al. (2013). The error bars of GRAVITY data are within the marker. The orbital parameters are listed in Table 2.
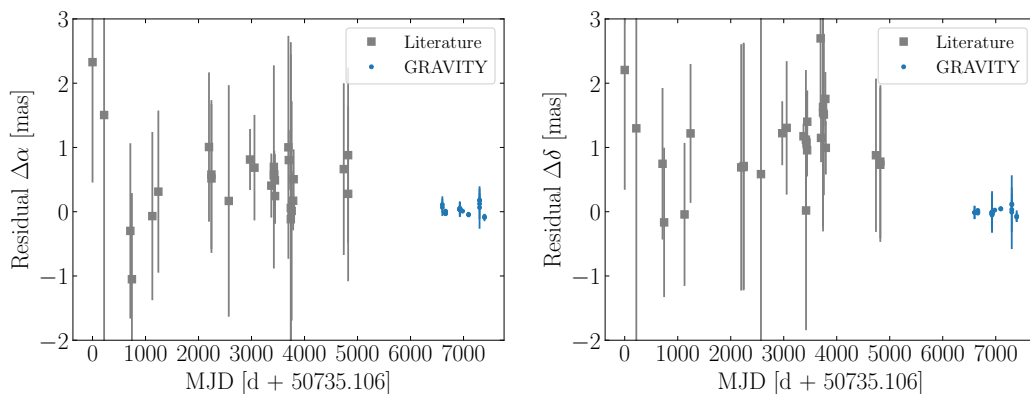
Fig. 8. Residuals of the $\Delta\alpha$ (left) and $\Delta\delta$ (right) positions from the orbit of θ^1 Ori C_2. The blue circles represent the residuals of GRAVITY data and their respective uncertainties. The grey squares are the residuals from non-GRAVITY observations. The RMS of the GRAVITY residuals is 0.07 mas for $\Delta\alpha$, and 0.05 mas for $\Delta\delta$.

Close et al. (2012) found a wide visual companion D_2 at a distance of $\sim 1.4'' = 580 \pm 10$ AU. Currently it is not clear if D_2 is physically bound to D_1. In order to estimate the mass of the companion, we used archival imaging data[2] of the Trapezium. We retrieved a NaCo image from 2005 and the corresponding calibration files. After calibrating the image with the NaCo reduction pipeline, we extracted the total flux of D_2 and Ori F as a magnitude reference and compared the flux D_2 with the flux of θ^1 Ori F. With the flux ratio, we determine a magnitude of $m_K = 11.69 \pm 0.06$. We assume that the extinction is comparable with the value for the primary ($A_V = 1.79$ Hillenbrand 1997)) and get $M_K = 3.4 \pm 0.1$. This corresponds to a mass of $\sim 1 \pm 0.1 \ M_\odot$.

A spectroscopic companion with a period of either 20.25 or 40.5 days was claimed by Vitrichenko (2002a). Another indication for a companion at a separation of 18.4 mas ($\approx 7.6 \pm 0.2$ AU) and with a flux ratio of 0.14 was suggested by Kraus et al. (2007). Grellmann et al. (2013) found indications for a structure at 2 mas or 4 mas, which is consistent with a close companion, but could not provide further constraints due to large uncertainties.

With GRAVITY, we detected a star θ^1 Ori D_3 with a flux ratio $f = 0.34 \pm 0.04$ at separations between 1.9 mas $\approx 0.79 \pm 0.2$ AU and 2.6 mas $\approx 1.08 \pm 0.2$ AU. The observed separations could correspond to the spectroscopic companion reported by Vitrichenko (2002a), since the inferred separations match quite well. However, we find no evidence for a companion at 18 mas. The trajectory of the detected companion does not favor a very eccentric orbit, i.e. it cannot be related to the detection claim of Kraus et al. (2007). The positions of D_3 are plotted in Figure 9. We calculate the apparent magnitude of D_3 to be 6.9 ± 0.3 mag and use $A_V = 1.79$ (Hillenbrand 1997) to estimate a mass of $6 \pm 1 \ M_\odot$ and a B spectral type. This agrees with Allen et al. (2017), who determined that the temperature of the spectroscopic companion of D_1 has to be ~ 20000 K, which corresponds to $\sim 7 \ M_\odot$. The determined orbital parameters are shown in Table 3. The angles ω and Ω are not well constrained. With the orbit and a distance of 414 ± 7 pc (Menten et al. 2007; Reid et al. 2014), we get a system mass of $21.68 \pm 0.05 \ M_\odot$. This corresponds to a companion mass of $\sim 6 \pm 1 \ M_\odot$ and a primary mass of $\sim 16 \pm 1 \ M_\odot$. Our data scatter with an RMS of 0.02 mas for $\Delta\alpha$ and 0.03 mas for $\Delta\delta$ (see Figure 10).

We set a 3σ detection limit with CANDID, excluding companions with $\Delta m < 2.5$ ($\approx 2.8 \ M_\odot$) in a range of 1.70–8.3 AU. For the 8.3–16.6 AU range the detection limit is $\Delta m = 3.9$ ($\approx 1.9 \ M_\odot$) and for 16.6–46.8 AU we set a limit of $\Delta m = 4.4$ ($\approx 1.9 \ M_\odot$).

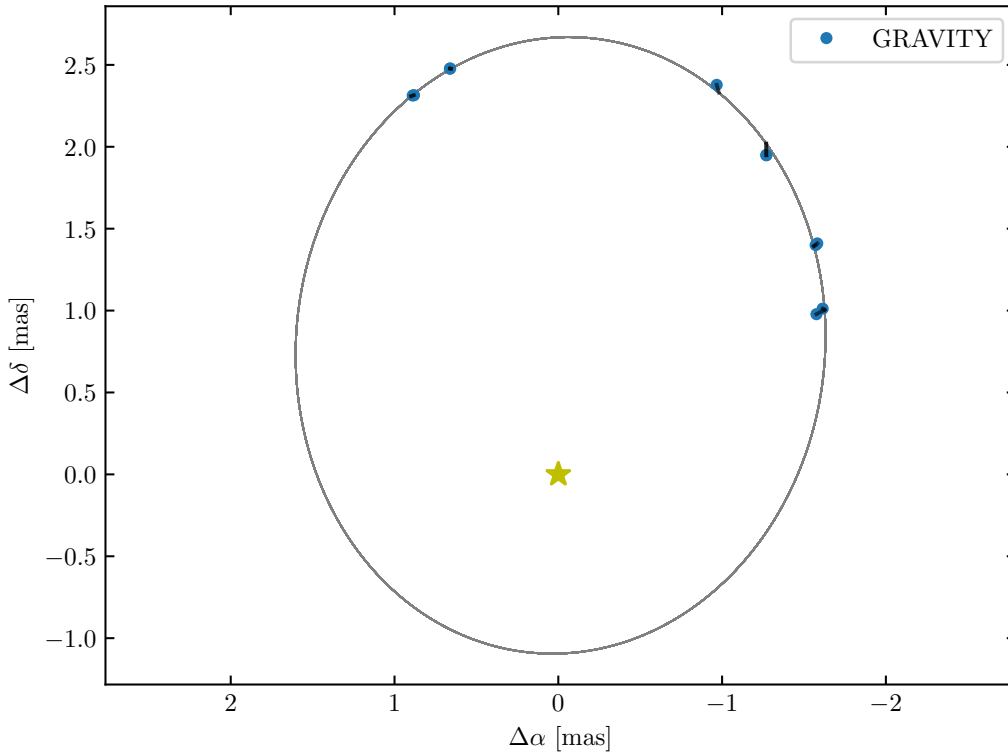[2] Based on data obtained from the ESO Science Archive Facility under request number 338322, ESO programme 274.C-5036(A).

Fig. 9. Positions of the newly detected θ^1 Ori D$_3$ around the primary D$_1$ at (0,0). The orbital parameters are listed in Table 3.
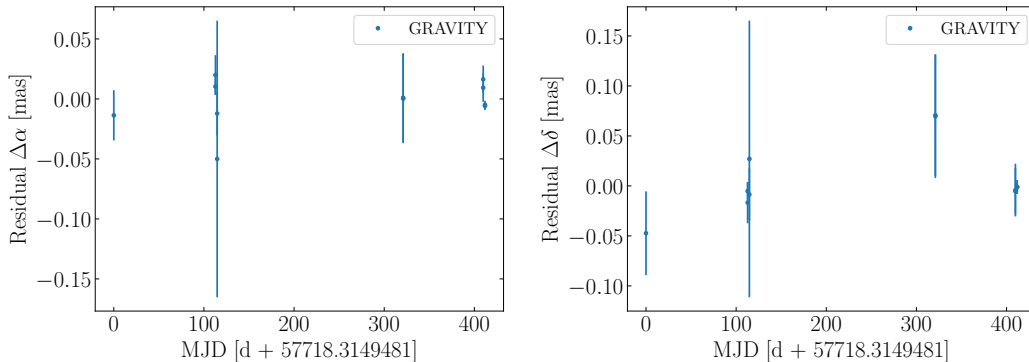

Fig. 10. Residuals of the $\Delta\alpha$ (left) and $\Delta\delta$ (right) positions from the fitted orbit of θ^1 Ori D$_3$. The RMS of the residuals is 0.02 mas for $\Delta\alpha$ and 0.03 mas for $\Delta\delta$.

4.1.5. θ^1 Ori E (Brun 584, TCC 40, Parenago 1864)

θ^1 Ori E is the second-strongest X-ray source in the Trapezium, exceeded only by θ^1 Ori C (Ku et al. 1982). Its K-magnitude is 6.9 (Muench et al. 2002) and Morales-Calderón et al. (2012) determined a spectral type of G2IV. The extinction is $A_V = 3.8$ (Feigelson et al. 2002).

Costero et al. (2006) and Herbig & Griffin (2006) discovered θ^1 Ori E to be a double lined spectroscopic binary, which consists of two approximately identical stars. Herbig & Griffin (2006) concluded that the components of θ^1 Ori E are located in the G-K region, but otherwise do not resemble typical T Tauri stars. They assumed masses of 3–4 $M_\odot$. Costero et al. (2008) determined a period of $P = 9.89520 \pm 0.00069$ d and a mass ratio $q = 1.004 \pm 0.018$. The period corresponds to a semi-major axis of 0.22 mas or 0.091 ± 0.001 AU. They also concluded that the binary system is escaping the Trapezium Cluster. Morales-Calderón et al.

Orbital parameter	This work
a [mas]	1.86 ± 0.06
P [yr]	0.1452 ± 0.0002
e	0.43 ± 0.03
τ	2017.101 ± 0.001
Ω [°]	346 ± 24
ω [°]	166 ± 27
i [°]	160 ± 12

Table 3. Orbital parameters of the best fit for the positions of θ^1 Ori D_3. 1.86 ± 0.06 mas correspond to 0.77 ± 0.03 AU at 414 ± 7 pc distance.

(2012) determined masses of 2.81 ± 0.05 $M_\odot$ and 2.80 ± 0.05 $M_\odot$. The eclipsing companions cannot be resolved with GRAVITY. We did not find evidence for further companions.

With CANDID, we set a 3σ detection limit of $\Delta m = 2.8$ (≈ 1.8 $M_\odot$) for 1.70–8.3 AU. For 8.3–16.6 AU the limit is $\Delta m = 3.9$ (≈ 1.4 $M_\odot$). In the range of 16.6–46.8 AU, we exclude companions with $\Delta m = 4$ (≈ 1.4 $M_\odot$).

4.1.6. θ^1 Ori F (Brun 603, TCC 72, Parenago 1892)

θ^1 Ori F is a B8-type star (Herbig 1950) with a magnitude in K-band of 8.38 (Muench et al. 2002). Studies by Petr et al. (1998) and Simon et al. (1999) did not detect companions with a separation ≥ 55 AU. We did not find any values for the extinction of θ^1 Ori F in the literature. With the method described in Section 4.1.2, we estimate a lower mass limit of 2.2 $M_\odot$. The typical mass for an B8-star is ~ 2.8 $M_\odot$ ((Allen & Cox, 2000, p. 150, p. 388; Salaris & Cassisi, 2005, p. 130), thus we estimate a mass range of 2.2–2.8 $M_\odot$ for θ^1 Ori F.

With the recent GRAVITY data, we can place a 3σ detection limit of $\Delta m = 1.75$ (≈ 1.5 $M_\odot$) in the range of 1.70–8.3 AU using CANDID. For the range 8.3–16.6 AU, we set a limit of $\Delta m = 2.6$ (≈ 1.4 $M_\odot$), and for 16.6–46.8 AU we get $\Delta m = 2.89$ (≈ 1.2 $M_\odot$).

4.2. Orion Nebula Cluster stars

The following stars are not strictly members of the Trapezium Cluster. However, they reside within 2.6 pc and belong to the youngest and most massive stars of the ONC. The apparent K-magnitudes are in the range of 4.49 to 11.05.

4.2.1. θ^2 Ori A (HD 37041, Brun 682, Parenago 1993)

θ^2 Ori A_1 is of spectral type O9.5IV (Sota et al. 2011) with a K-magnitude of 4.94 (Ducati 2002). Preibisch et al. (1999) estimated a mass of ~ 25 $M_\odot$. Simón-Díaz et al. (2006) determined a mass of 39 ± 14 $M_\odot$, an effective temperature of 35 000 K and a stellar radius of 8.2 ± 1.1 $R_\odot$.

θ^2 Ori A is a hierarchical system comprising a spectroscopic companion A_2 with a period $P = 20.9741 \pm 0.0028$ days (Aikman & Goldberg 1974; Abt et al. 1991). Assuming a circular orbit, this corresponds to a separation of $\sim 0.46 \pm 0.04$ AU (~ 1 mas). With the mass ratio $q \approx 0.35$ (Abt et al. 1991) the companion should be in the range of ~ 9–19 $M_\odot$.

Preibisch et al. (1999) discovered a visual companion A_3 at a separation of $0.38''$, corresponding to 157 ± 3 AU, and a mass ratio $q \approx 0.25$ (≈ 6–13 $M_\odot$). Grunhut et al. (2017) claimed the detection of another spectroscopic companion, but provided no orbital period or any further constraints on the companion.

With GRAVITY, we detect a companion at a separation of 1.3 mas ($\approx 0.538 \pm 0.011$ AU), likely the spectroscopic companion A_2. The observed positions are displayed in Figure 11.
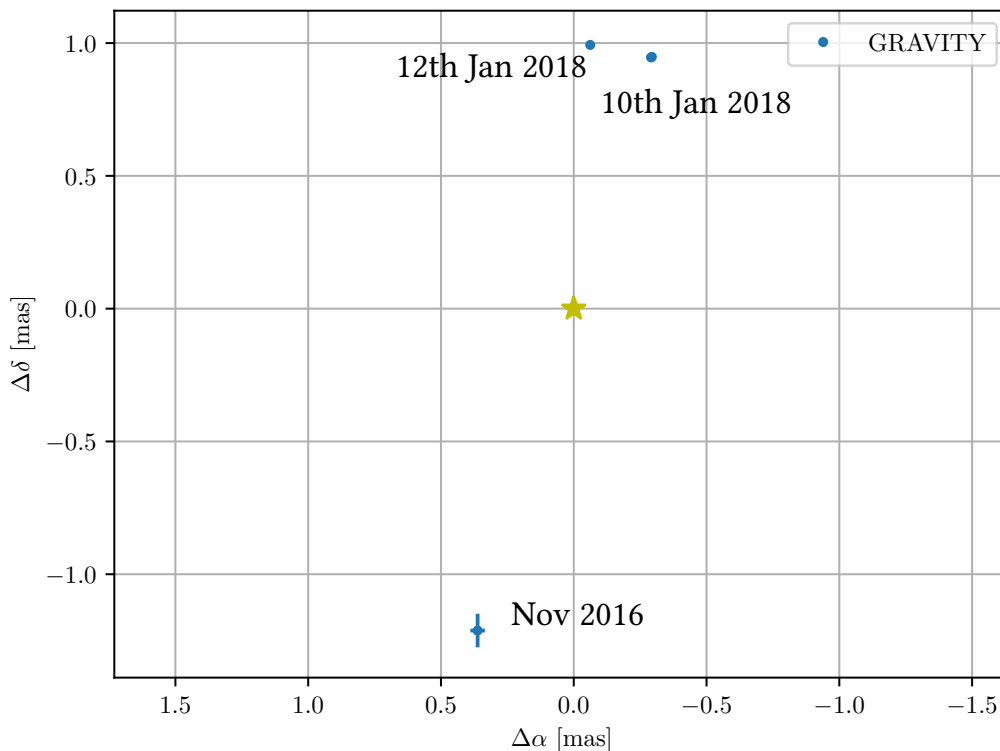
Fig. 11. Positions observed with GRAVITY of θ^2 Ori A_2, relative to $A_{1,3}$ at $(0,0)$.

We observe a flux ratio of $f = 0.52 \pm 0.04$, which corresponds to $m_K = 5.7 \pm 0.2$. Using $A_V = 1.12$ (Hillenbrand 1997) we find an absolute magnitude in K-band of $M_K = -2.5 \pm 0.2$. Comparing this magnitude with isochrones , we suggest a stellar mass of $\sim 10 \pm 2~M_\odot$ and an early B spectral type. This result is consistent with previous estimates.

With CANDID, we set a 3σ detection limit for the range of 1.70–8.3 AU of $\Delta m = 5.25$ ($\approx 1.6~M_\odot$) and a limit of $\Delta m = 6.2$ ($\approx 1.5~M_\odot$) for the range 8.3–16.6 AU. For 16.6–46.8 AU, we place a limit of $\Delta m = 6.47$ ($\approx 1.1~M_\odot$).

4.2.2. θ^2 Ori B (HD 37042, Brun 714, Parenago 2031)

θ^2 Ori B is a B2-B5 PMS star (Hillenbrand 1997) with a K-magnitude of 6.41 (Ducati 2002). Simón-Díaz et al. (2006) determined a mass of $9 \pm 3~M_\odot$ and a temperature of $29\,000 \pm 1000$ K together with a radius of $4.5 \pm 0.6~R_\odot$. The values agree with the results of Nieva & Przybilla (2014), who obtained $M = 14.8 \pm 3.4~M_\odot$, $T_{\text{eff}} = 29\,300 \pm 300$ K and $R = 4.3 \pm 0.4$.

Previous observations, e.g. Abt et al. (1991) or Preibisch et al. (1999), did not find indications for a companion star. GRAVITY observations made in January 2018 (see Table 1) allowed the detection of a companion at a separation of 95.8 mas $\approx 40 \pm 1$ AU with a small flux ratio of $f = 0.02 \pm 0.01$. This yields an apparent magnitude of 10.6 ± 1.3. Using $A_V = 0.73$ (Hillenbrand 1997), we obtain $M_K = 2.4 \pm 1.3$. A comparison with isochrones from Allen & Cox (2000, p. 150, p. 388) and Salaris & Cassisi (2005, p. 130) yields a mass estimate of $1.6 \pm 0.7~M_\odot$ and thus a late-A/early-F-type star.

Using CANDID, we set a 3σ detection limit of $\Delta m = 2.7$ ($\approx 1.9~M_\odot$) for the 1.70–8.3 AU and $\Delta m = 3.9$ ($\approx 1.6~M_\odot$) for 8.3–46.8 AU.

4.2.3. θ^2 Ori C (HD 37062, Brun 760, Parenago 2085)

θ^2 Ori C_1 is a B5V-type star (Samus' et al. 2017) with $m_K = 7.54$ (Cutri et al. 2003). Stelzer et al. (2005) determined an effective temperature $T_{\text{eff}} = 13800$. Comparing T_{eff} with typical values for main sequence stars (Salaris & Cassisi 2005, p. 130), we get a mass estimate of 4 ± 1 $M_\odot$, which agrees with the mass for B5-type stars.

Corporon & Lagrange (1999) detected a spectroscopic binary C_2 with a period $P \approx$ 13 days. This corresponds to a separation of 0.4 mas or 0.165 ± 0.003 AU, assuming a circular orbit.

With GRAVITY, we resolved for the first time a third companion C_3 at 38 mas, a projected separation of 15.7 ± 0.2 AU. The detected flux ratio is $f = 0.115 \pm 0.003$. With $A_V = 0.92$ (Hillenbrand 1997), this results in an apparent magnitude of 9.89 ± 0.07. The absolute magnitude is $M_K = 1.7 \pm 0.1$. Thus, a comparison with isochrones yields an estimate of 1.7 ± 0.2 $M_\odot$ and A spectral type.

4.2.4. NU Ori (HD 37061, Brun 747, Parenago 2074)

NU Ori$_1$ is a O9V-type star (Bragança et al. 2012) with a K-magnitude of 5.49 (Cutri et al. 2003). Hillenbrand (1997) determined a stellar mass of 16.3 $M_\odot$, whereas Landstreet et al. (2017) estimated $\sim$13 $M_\odot$ using effective temperatures but flagged it as particularly uncertain. Wolff et al. (2004) estimated a mass of $\sim$14 $M_\odot$, using the luminosity and the effective temperature but stated that there are systematic uncertainties from the evolutionary tracks of PMS stars. Thus, we assume that the mass of NU Ori$_1$ is in the range of 16 ± 3 $M_\odot$.

NU Ori has a spectroscopic companion NU Ori$_2$, discovered by Morrell & Levato (1991). Its orbital elements were determined by Abt et al. (1991), who found a period of $P = 19.1387 \pm 0.0028$ d. and the lower limit for the mass ratio $q = 0.19$. With a primary mass between 13 and 19 $M_\odot$, the lower limit for NU Ori$_2$ is 2.5–3 $M_\odot$. Assuming a circular orbit, we get a separation of 0.35 ± 0.03 AU.

Preibisch et al. (1999) discovered a companion star NU Ori$_3$ at $0.47''$. At a distance of 414 ± 7 pc (Menten et al. 2007; Reid et al. 2014), this corresponds to 195 ± 4 AU. The mass estimate is 1 $M_\odot$, with an upper limit < 4 $M_\odot$. Köhler et al. (2006) also detected a companion at $0.47(1)''$ with $\Delta m_K = 3.23 \pm 0.1$ mag. With this magnitude we are now able to estimate the stellar mass using the method described in Section 4.1.2. For an apparent K-magnitude of 8.7 ± 0.1, we get an absolute magnitude of $M_K = 0.4 \pm 0.1$ using the extinction $A_V = 2.09$ (Hillenbrand 1997). This yields a mass estimate of 2.4 ± 0.6 $M_\odot$ and thus an early A or late B-type star.

Grellmann et al. (2013) presumed another companion at either 20 mas or 10 mas separation. With our interferometric data, we found a companion NU Ori$_4$ at a distance of $d = 8.6$ mas $\approx 3.6 \pm 0.1$ AU with a flux ratio $f = 0.184 \pm 0.009$ (see Figure 12). This new detection is most likely a different star than the spectroscopic companion, because a period of 19 days translates to a distance of ≈ 0.9 mas, a factor of 10 smaller than the newly discovered separation of 8.6 mas. With the flux ratio of 0.184 ± 0.009, we get an apparent magnitude of 7.3 ± 0.1 and an absolute K-magnitude of -1 ± 0.1. This results in a mass estimate of 4 ± 1 $M_\odot$ and B spectral type.

We set a 3σ detection limit of $\Delta m = 3.8$ (≈ 2 $M_\odot$) for separations of 1.70–8.3 AU. For the range 8.3–46.8 AU, we determine a limit of $\Delta m = 4.6$ (≈ 1.8 $M_\odot$).
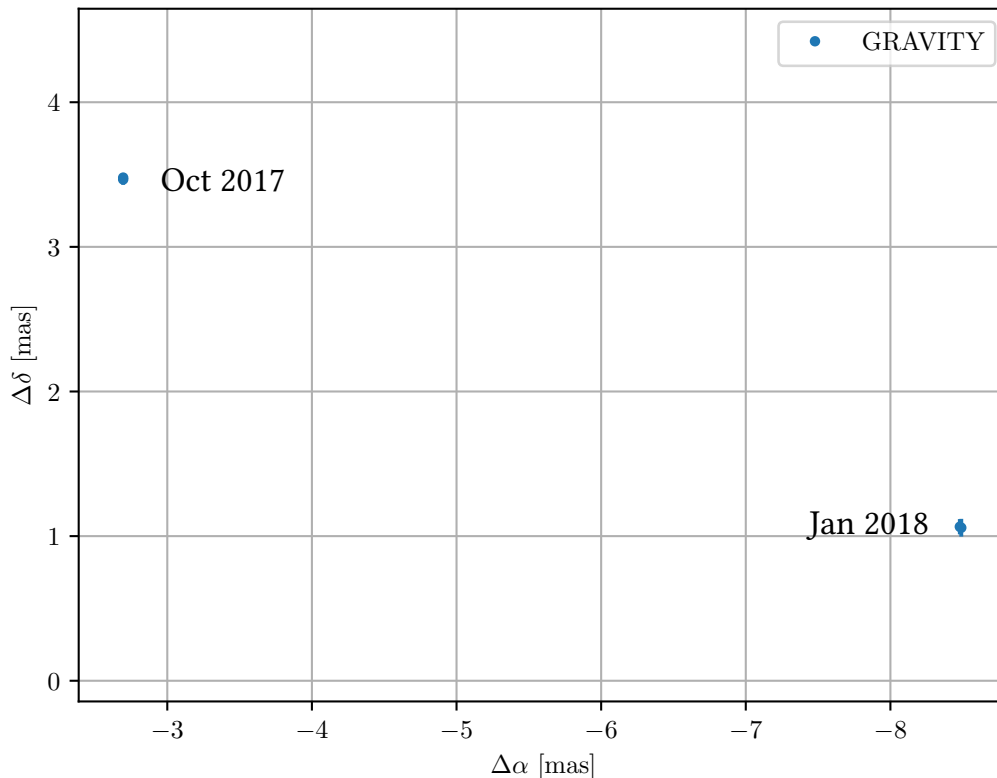
Fig. 12. Positions of NU Ori$_4$ with respect to NU Ori$_{1,2}$ at (0,0).

4.2.5. Brun 862 (Parenago 2208)

Brun 862 is a K3– M0I-type star (Hillenbrand 1997) with $m_K = 4.49$ (Cutri et al. 2003). To get a mass estimate, we take the calibration of MK spectral types for supergiants (luminosity class I) from Allen & Cox (2000, p. 390, Table 15.8.). For spectral type K3-M0, the corresponding mass is 13 $M_\odot$.

With GRAVITY observations from January 2018 (Table 1), we can either fit a companion Brun 862$_2$ at a separation of 0.29 ± 0.01 AU or fit a single star with a diameter of 0.33 ± 0.01 AU ($\sim 71\ R_\odot$), represented by a uniform disk. Both models fit the data equally well. For the first model the resulting flux ratio is $f = 0.26 \pm 0.04$. With $A_V = 6.78$ (Hillenbrand 1997), this would result in an absolute magnitude of $M_K = -2.9 \pm 0.4$. Assuming a main sequence star, we could estimate a mass of $\sim 10\ M_\odot$ and suggest a late O or early B spectral type. On the other hand, the latter model of a single extended star is more plausible, considering that Brun 862 is classified as a supergiant. We compare the radius of 71 $R_\odot$ with values from Levesque et al. (2005), who list K2 and K2.5 stars with $\sim 100\ R_\odot$. Thus, our determined radius agrees well with Levesque et al. (2005). We determine companion detection limits on a 3σ level for 1.70–46.8 AU of $\Delta m = 4.75$ ($\approx 2.2\ M_\odot$).

4.2.6. TCC 59

TCC 59 is a Young Stellar Object (YSO) with a protoplanetary disk (O'Dell & Wong 1996). It has a K-magnitude of 11.05 (Muench et al. 2002). For a lower mass limit, we compare the absolute K-magnitude with isochrones as described in Section 4.1.2, and get 1.5 $M_\odot$. We found no extinction measurements for this star, but as a YSO, its reddening in K-band is supposedly non-negligible. The color of (J-K) = 1.35 (Muench et al. 2002) is very red compared to the other stars in our sample. This indicates significant dust extinction or

intrinsics infrared excess due to, e.g., a circumstellar disk. Thus, we expect TCC 59 to be intrinsically brighter and more massive and only provide a lower limit. Close et al. (2012) claimed the detection of a companion star with 136 ± 3 mas ($\approx 56 \pm 2$ AU) separation.

In the data taken with GRAVITY in January 2018, we find signatures in visibilities and closure phases, but cannot find a good fit. Thus, it is not clear whether there is a companion star or whether the signatures result from a potential disk.

4.2.7. TCC 43

TCC 43 has a K-magnitude of 10.44 (Muench et al. 2002). Petr et al. (1998) and Simon et al. (1999) observed TCC 43 and did not find a companion star. With GRAVITY we see minor signatures in visibilities and closure phase, but cannot find a good fit. We set a lower mass limit of ~ 1.5 –1.7 $M_\odot$, i.e. an A or F-type using the method described in Section 4.1.2. We have no value for the extinction, therefore the star might be brighter and more massive.

With GRAVITY we can exclude companions in the 1.70–16.6 AU range with $\Delta m = 1.4$ (≈ 0.9 $M_\odot$) on a 3σ level. For separations of 16.6–46.8 AU, we place a limit of $\Delta m = 0.61$ (≈ 1.1 $M_\odot$).

4.2.8. LP Ori (HD 36982, Brun 530, Parenago 1772)

LP Ori is a B1.5V-type star (Samus' et al. 2017) with $m_K = 7.47$ (Cutri et al. 2003). Hillenbrand (1997) found an extinction $A_V = 1.47$ and a mass of 7.15 $M_\odot$. Reiter et al. (2018) determined a mass of $6.70^{+0.64}_{-0.37}$ $M_\odot$. Preibisch et al. (1999) and Abt et al. (1991) observed LP Ori but found no companion.

With GRAVITY we set a 3σ companion limit of $\Delta m = 2.12$ (≈ 1.9 $M_\odot$) for separations of 1.70–8.3 AU and $\Delta m = 2.87$ (≈ 1.5 $M_\odot$) for 8.3–46.8 AU.

4.2.9. HD 37115 (Brun 907, Parenago 2271)

HD 37115$_1$ is a B5-type star (Röser et al. 1994) with a K-magnitude of 7.13 (Cutri et al. 2003). Preibisch et al. (1999) estimated a mass of 5 $M_\odot$, Hillenbrand (1997) of 5.7 $M_\odot$ and Wolff et al. (2004) estimated a mass of 5.5 $M_\odot$. We take the mean mass 5.4 ± 0.4 $M_\odot$. Rio et al. (2016) determined $A_V = 5.9 \pm 0.3$.

Preibisch et al. (1999) found a companion at $\sim$890 mas separation, which corresponds to 368 ± 6 AU. The mass ratio is $\sim$0.29 and the estimated mass is $\sim$1.5 $M_\odot$ with an upper limit of < 5 $M_\odot$.

We do not detect a companion with GRAVITY but set a 3σ detection limit of $\Delta m = 2$ (≈ 2.2 $M_\odot$) for the range of 1.70–8.3 AU. For 8.3–16.6 AU we get a limit of $\Delta m = 2.42$ (≈ 1.9 $M_\odot$) and limit of $\Delta m = 3.24$ (≈ 1.5 $M_\odot$) for separation range 16.6–46.8 AU.

4.2.10. HD 37150 (Brun 980, Parenago 2366)

HD 37150 is a B3III/IV-type star (Houk & Swift 1999) with $m_K = 7.11$ (Cutri et al. 2003). We estimate a lower mass limit of 7 $M_\odot$, using the calibration table for MK spectral types from Allen & Cox (2000, p. 390, Table 15.8).

We do not detect a companion with GRAVITY. We set a 3σ detection limit of $\Delta m = 2.29$ (≈ 1.9 $M_\odot$) in the range of 1.70–8.3 AU and $\Delta m = 3.08$ (≈ 1.5 $M_\odot$) for separations of 8.3–46.8 AU.

4.3. Summary

We illustrate the observed companion systems in Figure 13 and provide a summary of all stellar systems and their properties in Table 4. Bold objects were observed with GRAVITY. For an overview of all observations, refer to Table 1. In total, 16 objects were observed, out of which eleven are confirmed multiple systems. This leads to a multiplicity fraction of $11/16 = 0.688$. All multiple systems combined have a total number of 22 confirmed companion stars. Thus, we get a companion fraction of $22/16 = 1.375$.

Brun 862 is a supergiant with no clear detection of a companion star. The evolutionary stage of Brun 862 differs greatly from the remaining stars in our sample. Additionally, the Gaia parallax of Brun 862 (1.690 ± 0.094, Gaia Collaboration et al. 2016, 2018; Luri et al. 2018) diverges significantly from the Gaia parallax of, e.g., θ^1 Ori C (2.472 ± 0.082). We will not include Brun 862 in the following discussion.
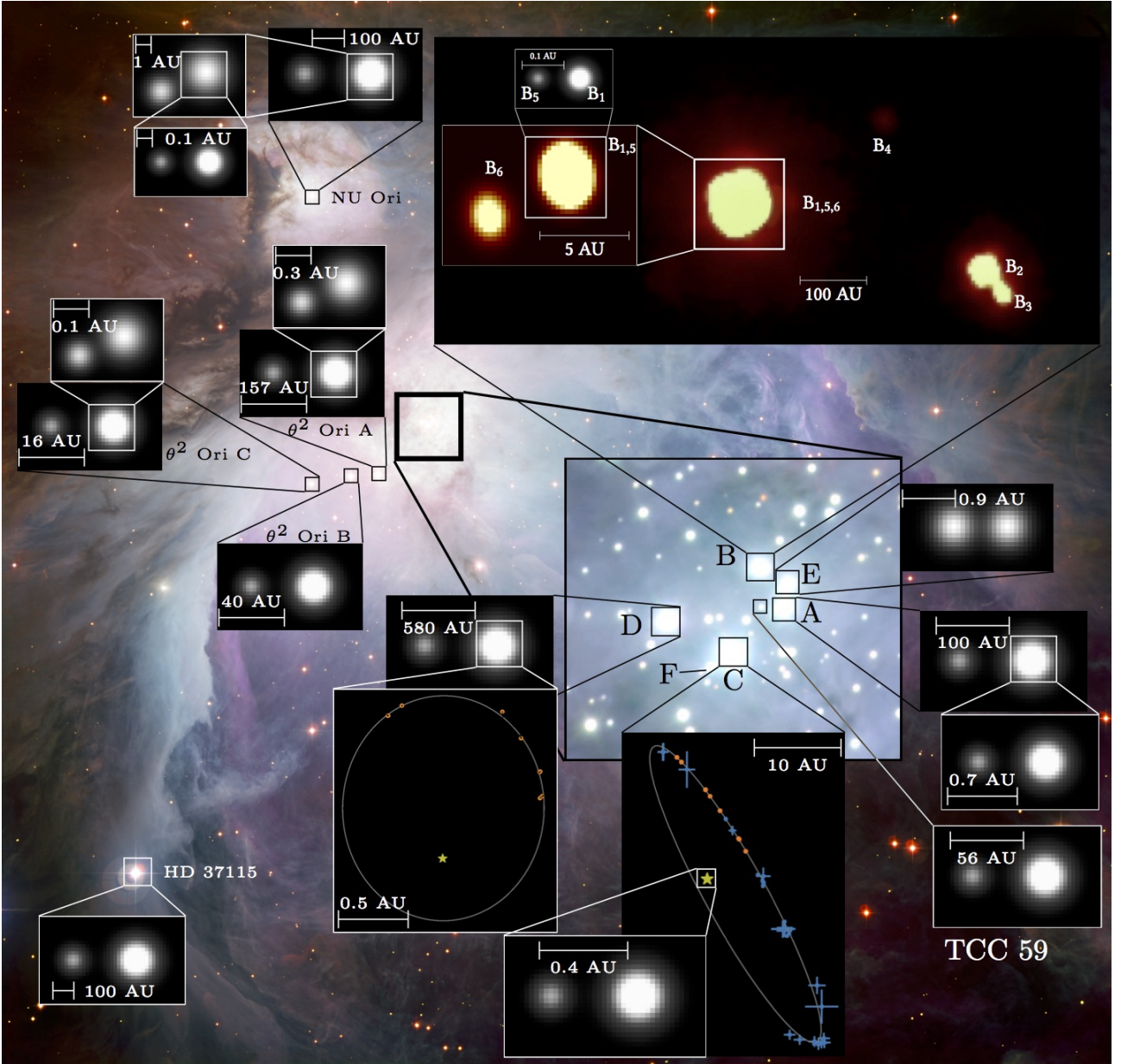
Fig. 13. Summary of the observed multiple systems in the Orion Nebula. We observed 16 multiple systems with a total number of 22 companion stars. The respective scales are indicated. The images of θ^1 Ori B are from actual obervational data, except for the spectroscopic B_1, B_5 system, which is only a representation. The orbital positions for θ^1 Ori D and θ^1 Ori C are the positions obtained in this work and from the literature. All remaining close up depiction of stars (gray) are only for illustrative purposes and were not created with observational data. The background image of the Orion Nebula was created by ESO/Igor Chekalin. The zoom of the Trapezium Cluster (θ^1) is a cut from ESO/M. McCaughrean et al. (AIP).

5. Discussion

Our sample comprises 15 objects, excluding Brun 862. Eleven of them are multiple systems with up to six members. With long baseline interferometry observations performed using GRAVITY, we close the gap between close spectroscopic companions and more distant visual companions. This yields a complete sample of companions for our observed systems down to our detection limit of 1.5–3 $M_\odot$.

5.1. Multiplicity

Duchêne & Kraus (2013) provided an overview of the multiplicity of stars. The multiplicity fraction MF is defined as

$$MF = \frac{N_{\mathrm{mult}}}{N_{\mathrm{mult}} + N_{\mathrm{single}}}, \tag{3}$$

where N_{mult}, the number of multiple systems, is divided by the total number of systems, namely the sum of multiple star and single star systems. The companion frequency or companion fraction CF is the average number of companions per target

$$CF = \frac{N_{\mathrm{comp}}}{N_{\mathrm{prim}} + N_{\mathrm{single}}}, \tag{4}$$

with N_{comp} as the number of companion stars, $N_{\mathrm{prim}} = N_{\mathrm{mult}}$ as the number of primary stars and N_{single} as the number of single stars.

We compare our resulting companion fraction with the values from Duchêne & Kraus (2013), Sana et al. (2014), and Moe & Di Stefano (2017), as shown in Figure 14. Generally, we notice a rising companion fraction for higher masses. For stars with 3–7 $M_\odot$, we obtain a companion fraction of 1 ± 0.6, which agrees well with Duchêne & Kraus (2013), and Moe & Di Stefano (2017). For 7–16 $M_\odot$, our companion fraction is 2.0 ± 0.9 and agrees with 1.0 ± 0.2 by Duchêne & Kraus (2013), and 1.6 ± 0.2 by Moe & Di Stefano (2017) within the error bars. We get a companion fraction of 2.3 ± 0.4 for stars > 16 $M_\odot$, which is nearly by a factor of two larger than the result 1.3 ± 0.2 obtained by Duchêne & Kraus (2013). Sana et al. (2014) presented the result of a survey of O stars and derived a companion fraction of 1.45 ± 0.5 for main sequence stars with companions at separations of 1–600 AU, which is comparable to our observed companion separations. Their survey covered companions up to separation ranges of 1–16 000 AU and yields a companion fraction of $2.18^{+0.3}_{-0.32}$ for O main sequence stars. We cannot assign companion stars at such large separations in the ONC, because the system would be unstable due to interactions with other cluster members. Still, our observed companion fraction of 2.3 ± 0.4, for separation ranges up to $\sim$600 AU, agrees with the result of $2.18^{+0.3}_{-0.32}$ by Sana et al. (2014), for their full separation range of 1–16 000 AU. Our result is also in good agreement with the companion fraction of 2.1 ± 0.3, determined by Moe & Di Stefano (2017) for O-type stars with masses > 16 $M_\odot$.

The multiplicity fraction or multiplicity frequency (MF) is the number of multiple systems divided by the number of targets, as in Equation (3). We compare our MF with previous results in Figure 15. For stars > 3 $M_\odot$, the MF of our sample is higher than the lower limits from Duchêne & Kraus (2013). For the mass range ≥ 16 $M_\odot$ we obtain a MF of 100%. This agrees with the MF $1^{+0.00}_{-0.05}$ from Sana et al. (2014) and $1^{+0.00}_{-0.2}$ from Moe & Di Stefano (2017) for main sequence stars of type O. We consider our sample to be complete for stars > 3 $M_\odot$. For each mass range we use $1/\sqrt{N}$ as uncertainty estimate. Thus, the actual MF of stars < 3 $M_\odot$ is probably higher than our biased value.
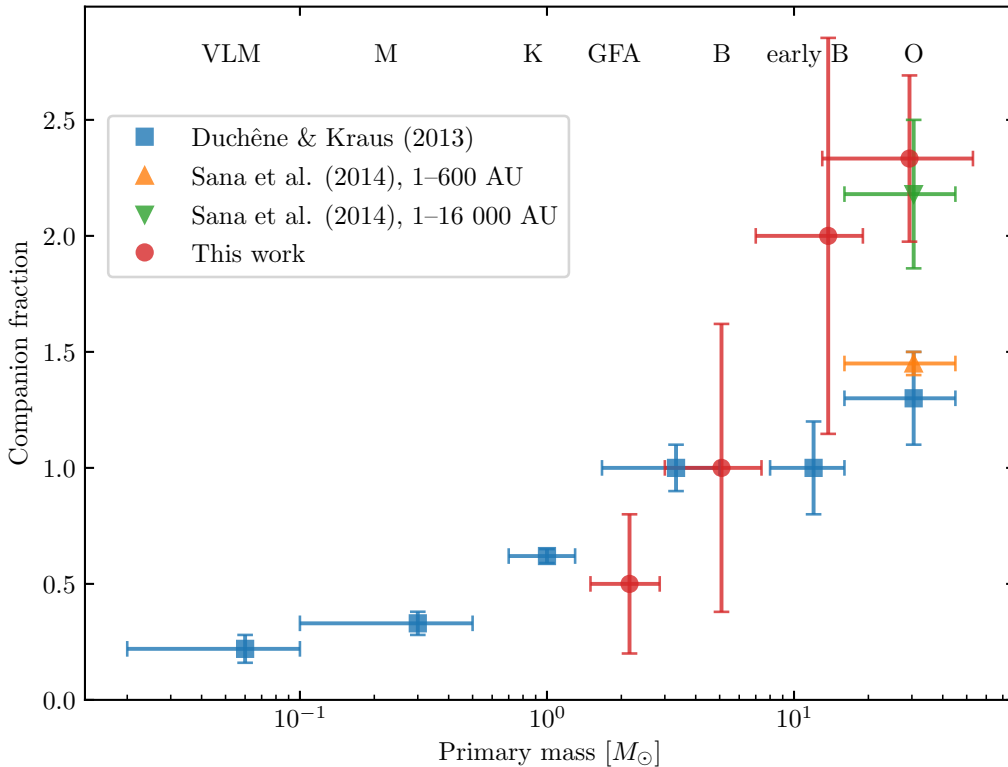
Fig. 14. The companion fraction CF as measured with GRAVITY for mass ranges $< 3\ M_\odot$, 3 $-7\ M_\odot$, $7\ -16\ M_\odot$, $> 16\ M_\odot$ (red circles). The values from Duchêne & Kraus (2013) for very low mass stars (VLM), spectral types M, K, G, F, A, B, early B and O (from left to right), and the values from Sana et al. (2014) for O stars are plotted for reference. The companion fraction of Sana et al. (2014) depends on the considered separation range for companions. A range $\lesssim 600$ AU is similar to the separations in our sample.

5.2. Initial Mass Function

In our discussion of the initial mass function, we will only consider stars $\geq 3\ M_\odot$. This corresponds to our most conservative detection limit (see Table 4). Down to this limit, we consider our sample to be complete for separations $\lesssim 600$ AU.

The initial mass function (IMF) describes the frequency of stars with masses in a given mass bin $(m + dm)$ at birth. For a detailed review of the IMF see Bastian et al. (2010); Scalo (1986) or Kroupa et al. (2013) and references therein. Salpeter (1955) suggested a power law of the form:

$$\Phi(\log m) = \frac{dN}{d \log m} \propto m^{-\Gamma}, \tag{5}$$

with m as the mass, N as the number of stars in the mass range $\log m + d \log m$ and $\Gamma = 1.35$. The IMF can also be written in the form of

$$\xi(m) = \frac{dN}{dm} \propto m^{-\alpha}, \tag{6}$$

with the relation

$$\xi(m) = \frac{dN}{dm} = \frac{1}{m \log 10} \frac{dN}{d \log m} = \frac{\Phi(\log m)}{m}, \tag{7}$$

yielding $\alpha = \Gamma + 1$. For $> 1\ M_\odot$, Muench et al. (2002) suggested $\Gamma = 1.21$ for the Trapezium. More generally, Kroupa (2001) estimated $\Gamma = 1.3 \pm 0.7$, which agrees with Chabrier (2003)
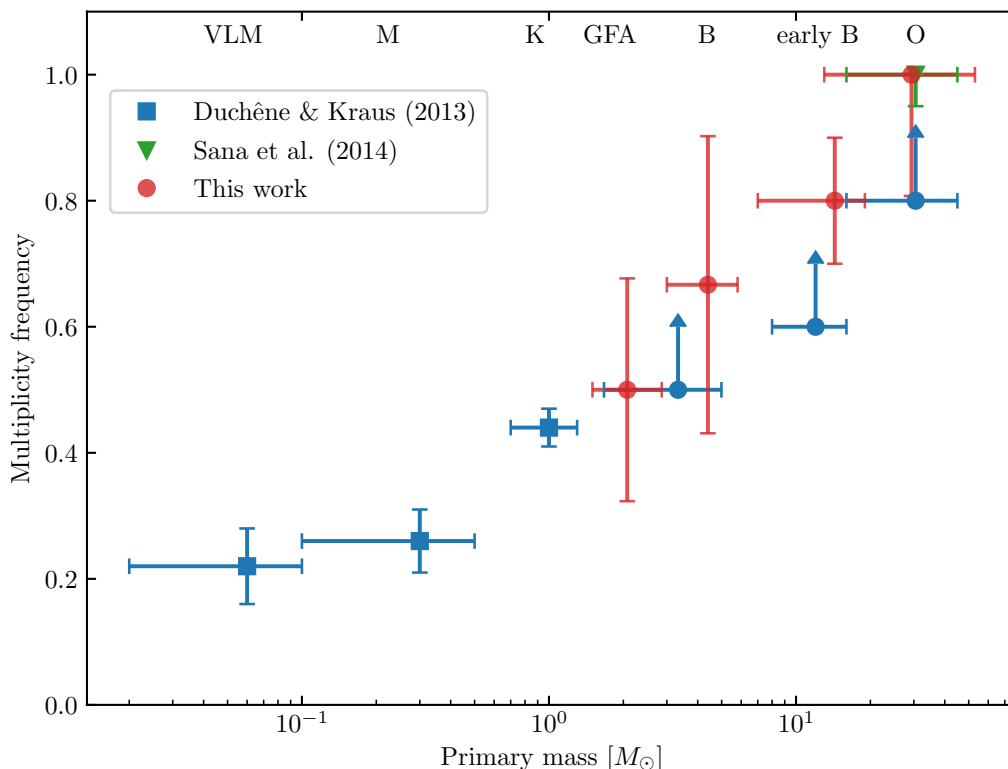
Fig. 15. The multiplicity fraction MF as measured with GRAVITY for mass ranges $< 3\ M_\odot$, $3 -7\ M_\odot$, $7 -16\ M_\odot$, $> 16\ M_\odot$ (red circles). The values from Duchêne & Kraus (2013) for the whole mass range of $\lesssim 1\ M_\odot$ to O stars and the values from Sana et al. (2014) for O stars are plotted for reference. For each mass range we use $1/\sqrt{N}$ as uncertainty estimate.

and their result of $\Gamma = 1.3 \pm 0.3$ for young clusters. Kroupa et al. (2013) noted that a good estimate for the intermediate mass regime $1 < m < 8\ M_\odot$ is difficult, but suggested $\Gamma = 1.3$ as the best estimate. E.g. Muench et al. (2002); Da Rio et al. (2010) concluded that the IMF of the ONC is described by a Salpeter IMF for stars $\geq 0.6\ M_\odot$. Further measurements of the exponent focused mainly on the low mass regime ($\leq 1\ M_\odot$), see e.g. Mužić et al. (2017), Drass et al. (2016), Da Rio et al. (2012) or Muench et al. (2002).

We bin our observed distribution of masses for all stars and compare the histogram with a model IMF suggested by Kroupa (2001) and Chabrier (2003), as shown in Figure 16. The distribution is calculated by integrating the probability density $f(m) = dN/dm \propto m^{-2.3\pm0.3}$. The cumulative distribution is depicted in Figure 17. The observed mass distribution of the most massive ONC stars — including their companions — agrees remarkably well with the IMF for field stars proposed by Kroupa (2001) and Chabrier (2003). This illustrates the importance of resolving companions to get a complete sample. Counting only the primary component would result in a smaller power-law index and yield the impression that massive stars were distributed differently than in the field. We estimate the uncertainties in Figure 16 to be $\pm 1/\sqrt{N}$ for each bin.

5.3. Distribution of Masses and Mass Ratios

We compare stellar masses, mass ratios q, and separations of companions by plotting different quantities against each other. It is important to stress that our sample is only complete for masses $\geq 3\ M_\odot$. This leads to a bias, especially for the mass ratio, since we will be missing stars at the low mass end. We present our results here based on the observed stars, keeping in mind that we are missing a part of the population. Furthermore,
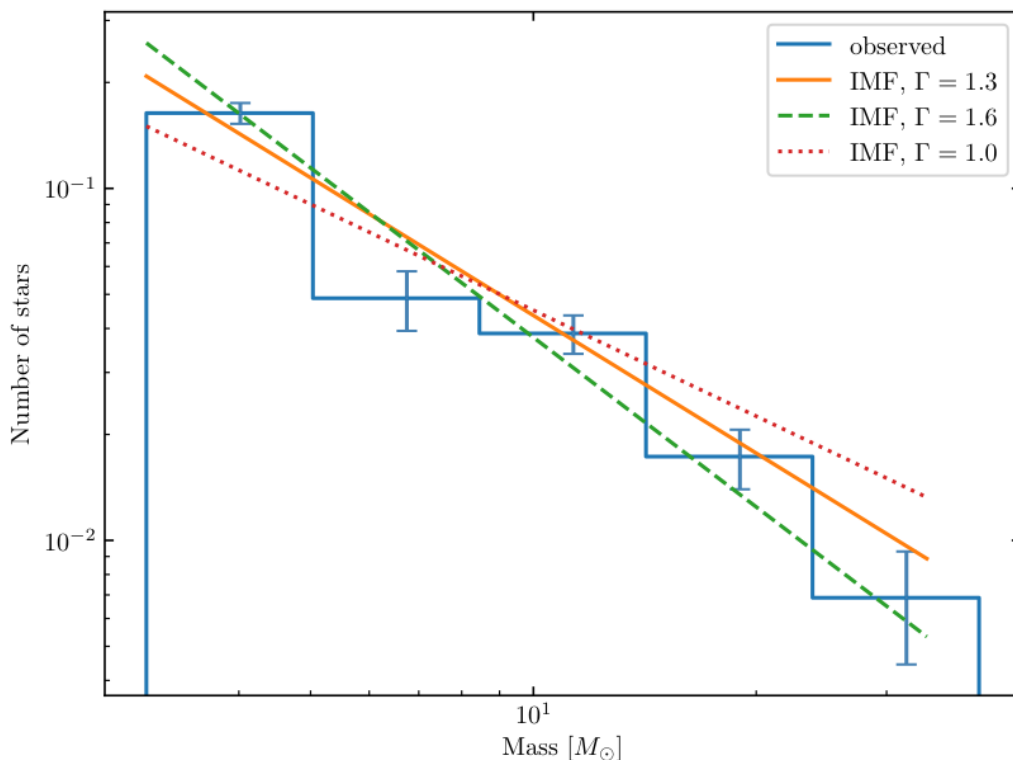
Fig. 16. Normalized histogram of stars per mass. The observed distribution is compared with distribution functions of Chabrier (2003). We estimate the uncertainties to be $\pm 1/\sqrt{N}$ per bin.

photometric mass estimates rely strongly on evolutionary models and can comprise many uncertainties. It is only possible to provide a precise system mass if the Orbit is known.

First, we look at the primary mass and the corresponding mass ratios for all companions. In Figure 18, the mass ratio per primary mass is displayed. Different markers represent different systems. Additionally, the color categorizes the companions according to their order, going from the innermost to the outermost. We find high mass ratios $\gtrsim 0.6$ only for primary masses $\lesssim 8\ M_\odot$. For stars with masses $\gtrsim 8\ M_\odot$, the mass ratio is $\lesssim 0.5$. In every system, the most massive companion is either the closest or second-closest companion to the primary star.

The most massive companions $\gtrsim 8\ M_\odot$ belong to the most massive primary stars with $\geq 30\ M_\odot$. They have a mass ratio in the range 0.3–0.4. We see no tendency for the companion to have a high mass similar to the primary — e.g. $q \approx 1$ — if the primary is a high mass star. This disagrees with the result of Chini et al. (2012), who found that most massive stars have companions of similar mass. In our sample, only intermediate mass stars with masses between 3–8 $M_\odot$ have a $q \gtrsim 0.5$.

A histogram of the mass ratio q is shown in Figure 19 and the cumulative distribution in Figure 20. We find a clear preference for small mass ratios, hence large mass differences. The most common values are ≤ 0.2. Our distribution is biased, because our sample is incomplete for stars with masses $< 3\ M_\odot$. Furthermore, small mass ratios ($q < 0.01$) are hard to detect with interferometry and imaging due to the extreme contrast ratios. In other words, any survey will be incomplete at low q. The underlying distribution is likely to show an even stronger preference for low q. We want to compare our distribution with other samples. Duchêne & Kraus (2013) stated that a power law is not an ideal representation for most distributions of q, but it is still the best way to compare multiple systems with different mass ranges. Thus, we follow their approach and fit our distribution with a power law
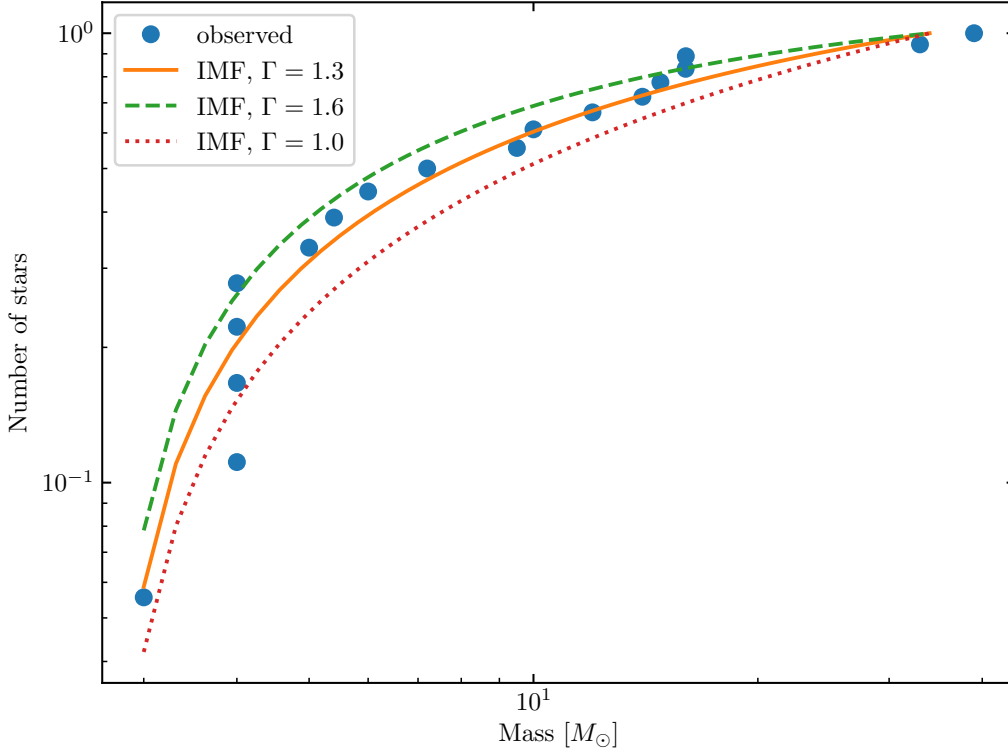
Fig. 17. Cumulative distribution of stars per mass with the respective distribution functions.
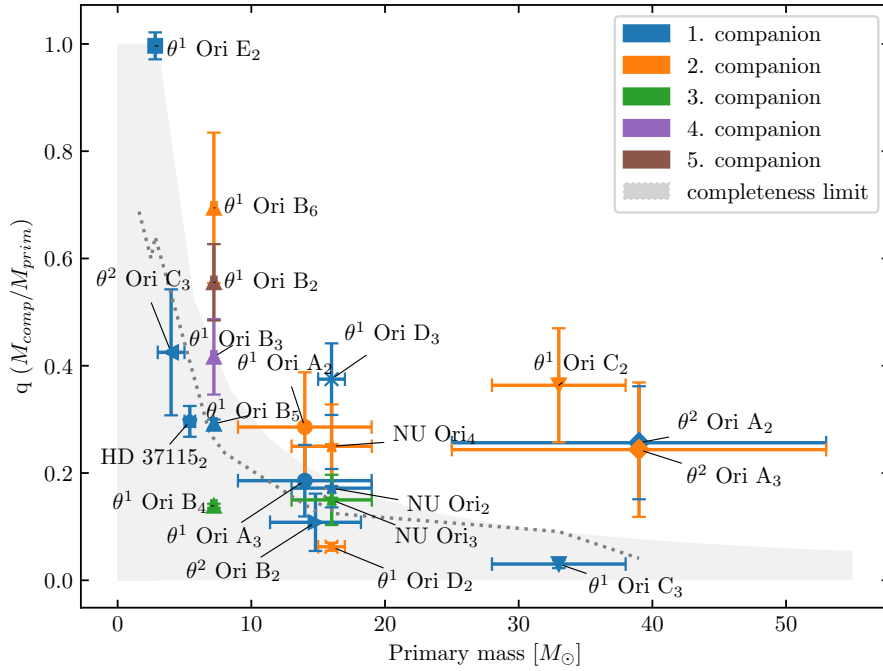
Fig. 18. Mass ratio per primary mass; each system is represented by a different marker. The colors indicate the companion order, starting from the innermost. Thus, the first companion (blue) means the companion closest to the primary, the second companion (orange) means the second-closest companion, etc. The gray area indicates the mass range $\leq 3\ M_\odot$, for which we are no longer complete. The gray dotted line marks the individual mass limits for each system as given in Table 4.
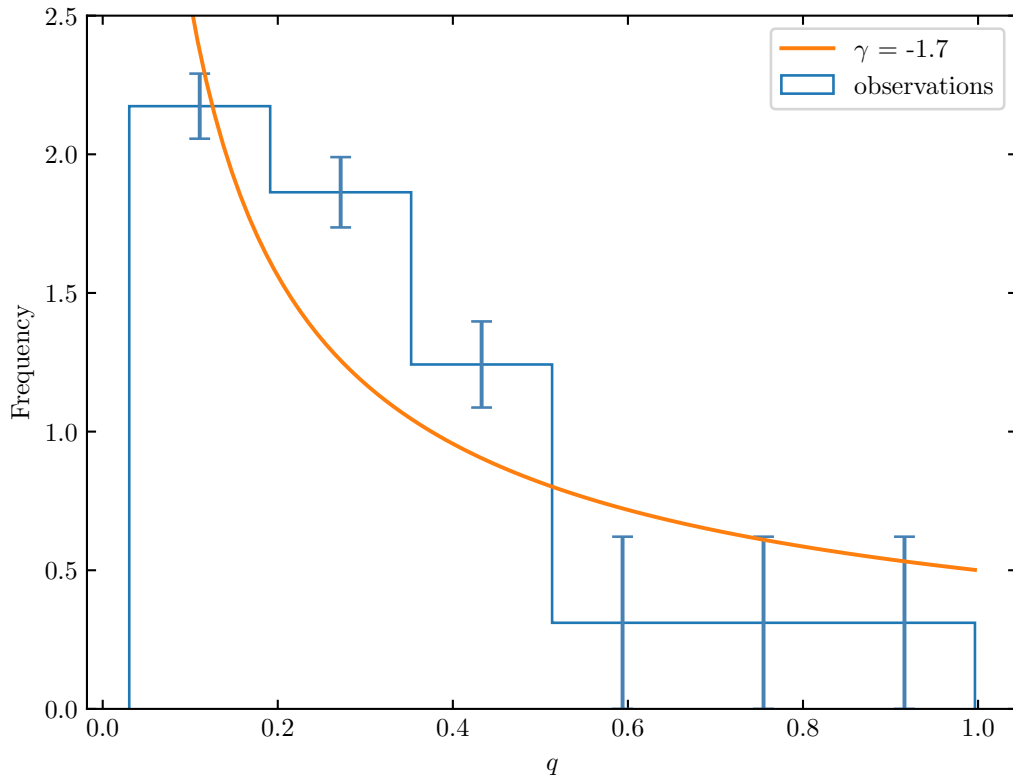
Fig. 19. Normalized histogram of all mass ratios q and the best fit curve of a power law $\propto q^{\gamma} = q^{-1.7 \pm 0.3}$.
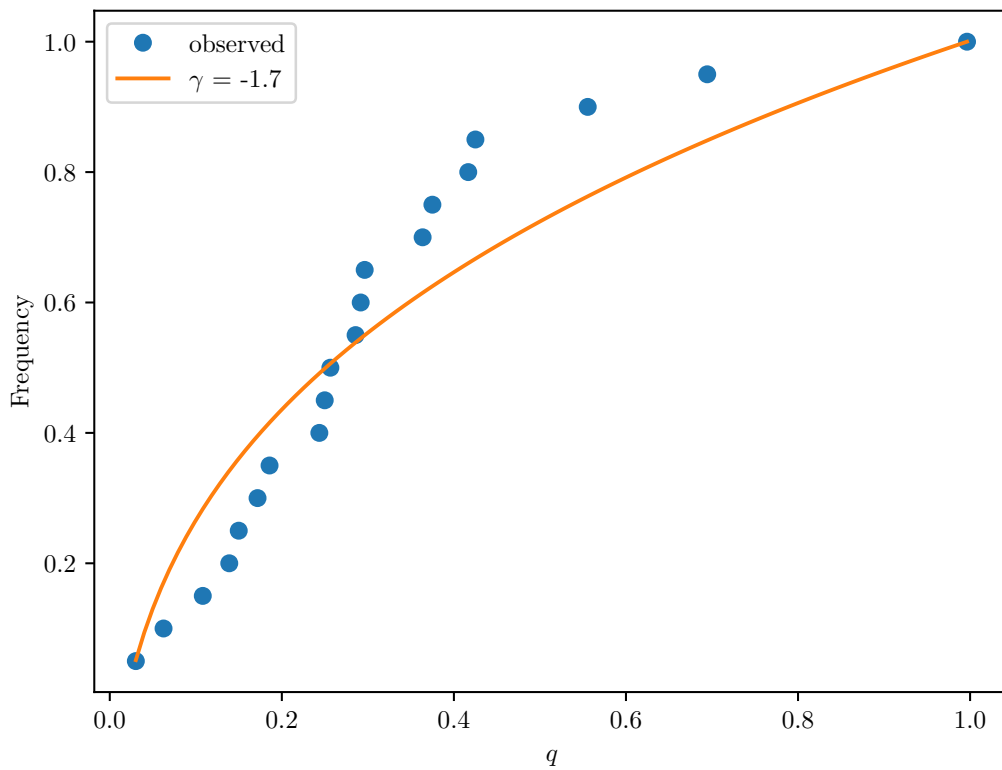
Fig. 20. Cumulative distribution of all mass ratios q and the best fit curve of a power law $\propto q^{\gamma} = q^{-1.7 \pm 0.3}$.
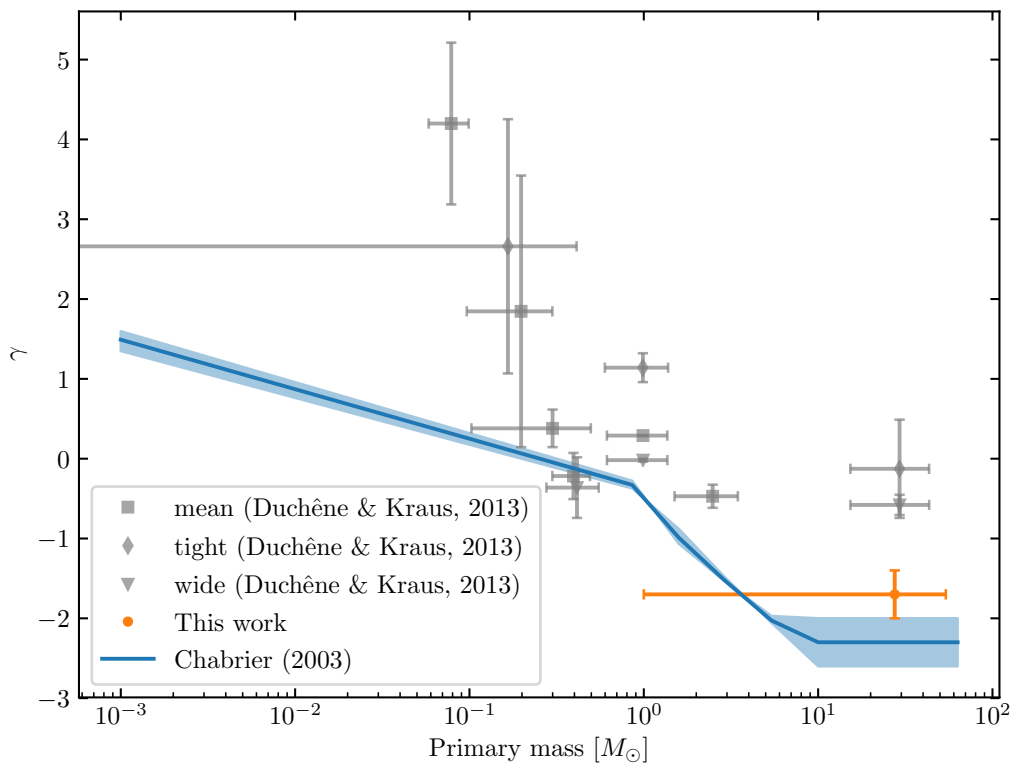
Fig. 21. The power-law index γ of the mass ratio distribution with $dN/dq \propto q^\gamma$ for different masses. The squares represent the fits of the overall population of multiple systems by Duchêne & Kraus (2013). The diamonds are the results for tight binaries (smaller separations than average) and the down-facing triangles the result for wide binaries (larger separations than average) by Duchêne & Kraus (2013). Our data is represented by a distribution with an index of -1.7 ± 0.3 (red circle). If the companion stars follow the IMF of Chabrier (2003), the index of q is equal to the index of the IMF with $\gamma = -2.3 \pm 0.3$, for companions with masses $1 \leq m_{\mathrm{comp}} \leq m_{\mathrm{primary}}$. The shaded area indicates the uncertainties of the IMF.

$dN/dq \propto q^\gamma$, similar to Section 5.2. Our distribution of q is best fitted by $\gamma = -1.7 \pm 0.3$ (see Figure 19). Moe & Di Stefano (2017) found values for γ of -0.5 ± 0.3 for stars with a period of 10 days, $\gamma = -1.7 \pm 0.3$ for stars with a period of 1000 days and masses > 5 $M_\odot$, and $\gamma = -2.0 \pm 0.3$ for stars with a period $\gtrsim 270$ years and masses > 5 $M_\odot$. Our sample consists of stars with periods ranging from a few days to > 1000 yr (see Table 4). These values agree well with our resulting γ of -1.7 ± 0.3. Thus, considering the uncertainties, our companion mass distribution can be described by an IMF with $\alpha = 2.3 \pm 0.3$. In Figure 19, we calculate γ for Chabrier (2003) by taking a primary mass and considering companions down to $q = 0.1$. For stars ≤ 1 $M_\odot$ the IMF follows a lognormal distribution. As soon as the primary mass is < 10 $M_\odot$, the lognormal distribution changes the companion mass distributions of companions ≤ 1 $M_\odot$. Hence, γ is no longer constant.

We compare our distribution of q with the distributions in Duchêne & Kraus (2013). Figure 21 shows γ for systems with different primary mass ranges. Our sample is in the range $\gtrsim 1$ $M_\odot$. The distributions by Duchêne & Kraus (2013) follow a nearly flat distribution $\gamma \lesssim 0.5$ for masses $\gtrsim 0.3$ $M_\odot$. We notice a steeper distribution in our sample with $\gamma = -1.7$ than Duchêne & Kraus (2013) for masses ≥ 3 $M_\odot$. If we assume that the companion mass follows an IMF, the index γ will correspond to the power-law index $\alpha = -\gamma$. Our result agrees within the uncertainties of an IMF according to Kroupa (2001) with $\alpha = 2.3 \pm 0.6$ and is consistent the exponent $1.90^{+0.37}_{-0.36}$ obtained by Schneider et al. (2018).

In Figure 22, we compare the resulting mass ratios q with the corresponding companion separation. We notice no significant correlation between q and separation. The only system
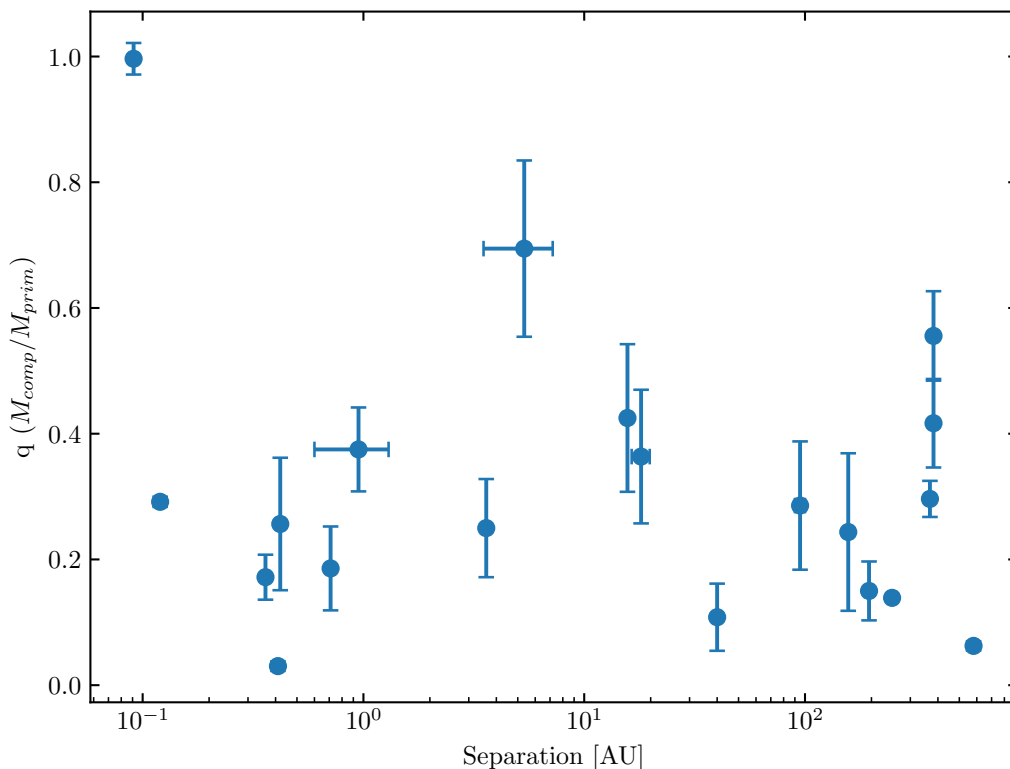
Fig. 22. Separation in AU in a logarithmic scale per mass ratio q.

with $q \approx 1$ has a small separation of ≈ 0.09 AU. But we also find systems with a separation of ~ 400 AU and $q \sim 0.6$, which is one of the highest mass ratios in our sample.

Figure 23 shows the companion separation per system. There appears to be a preferred separation range for companion stars. We find eight companions within 1 AU, thus we notice a tendency for binaries with separation < 1 AU, which are typically spectroscopic binaries. Then there are only two companions within 1–10 AU. The next five companions cover the range 10–100 AU. This means, there are as many companions within 1–100 AU as there are within 0.08–1 AU.

We present the distribution of companion separation in Figure 24. Duchêne & Kraus (2013) described the orbital period distribution of OB stars with a peak at ~ 0.2 AU and with a decreasing power-law tail for > 1 AU. They also determined the distribution for A stars, which is bimodal. A qualitative sketch is provided in Figure 24 in comparison to the distribution of our observed separations. We also find a peak for companions in short distance but in a range up to ~ 4 AU. Furthermore, we notice a decrease between 1–100 AU and a second peak at 400–600 AU, i.e. a bimodal distribution. Our distribution more closely resembles that of the Duchêne & Kraus (2013) distribution for A stars, even though our sample consists mainly of O and B stars (see Table 4).

On the left of Figure 25, we compare the companion mass with separation. There appears to be no trend for the companion mass over the separations. Finally, we compare the multiplicity with the system distance from θ^1 Ori C as shown in Figure 25 on the right. In a comparable plot by Preibisch et al. (1999), there was a trend towards fewer companions for more distant objects from θ^1 Ori C. We do not observe such a trend in our sample. It is possible that stars move away from their original birthplace, so that their location and multiplicity differs from their primordial distribution. It is also possible that the multiplicity was not triggered by winds and outflows of θ^1 Ori C, but is universal. It could also depend on the stellar density of the cluster in general.
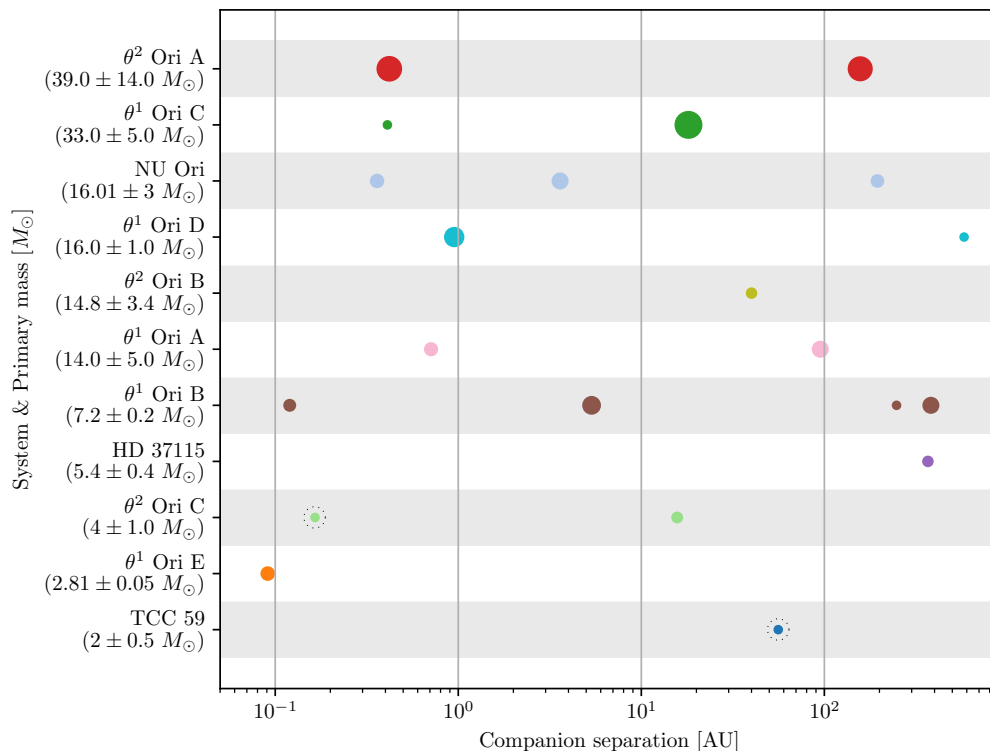
Fig. 23. The companion separation per system with given primary mass in $M_\odot$. In the range between 1–100 AU, we are sensitive down to 3 $M_\odot$. There are equally many companion stars in the range 0.1–1 AU as in the range 1–100 AU. The colors indicate different systems, the marker size scales with the square root of the companion mass. The dotted circles indicate missing information about the mass of the first companion of θ^2 Ori C and TCC 59.

5.4. Comparison with Star Formation Models

We compare our results with star formation models. The core accretion model predicts that the multiplicity and companion fraction rises with stellar mass (Clarke 2001). Disk fragmentation predicts low mass companions at 100-1000 AU (Kratter & Matzner 2006; Krumholz 2016). Krumholz (2006) suggested that high temperatures stabilize the core, leading to less fragmentation, even for high mass cores. This results in a small amount of massive protostars and a preference for binaries with high mass components. These massive components of high mass stars make the mass distribution of companion stars top-heavy. The massive core fragment also needs a larger volume to form, thus, we expect a correlation between system mass and separation.

Competitive accretion predicts a dependence of the separation r on the system mass M. In a turbulent medium, the relation is $r \propto M^{-2}$ (Bonnell & Bate 2005). The result of competitive accretion is a cluster with a large range of masses, where high mass stars are formed at the center of the cluster core (Bonnell 2005b) with close high mass companions. The companion frequency rises with stellar mass, see e.g. Peter et al. (2012).

Binaries with low masses and wide separations continue to accrete mass and evolve to a close high mass binary. The result is a close system with two massive components (Bonnell & Bate 2005). The fragmentation of clouds leads to clusters similar to the Trapezium Cluster (Bonnell & Bate 2005; Bonnell 2005a,b). The model also predicts three-body captures, where a high mass primary star with a low mass companion captures a massive wide companion star (Bonnell 2005b). The massive companion star absorbs most of the binding energy of the low mass star and the separation between the two high mass components shrinks. The
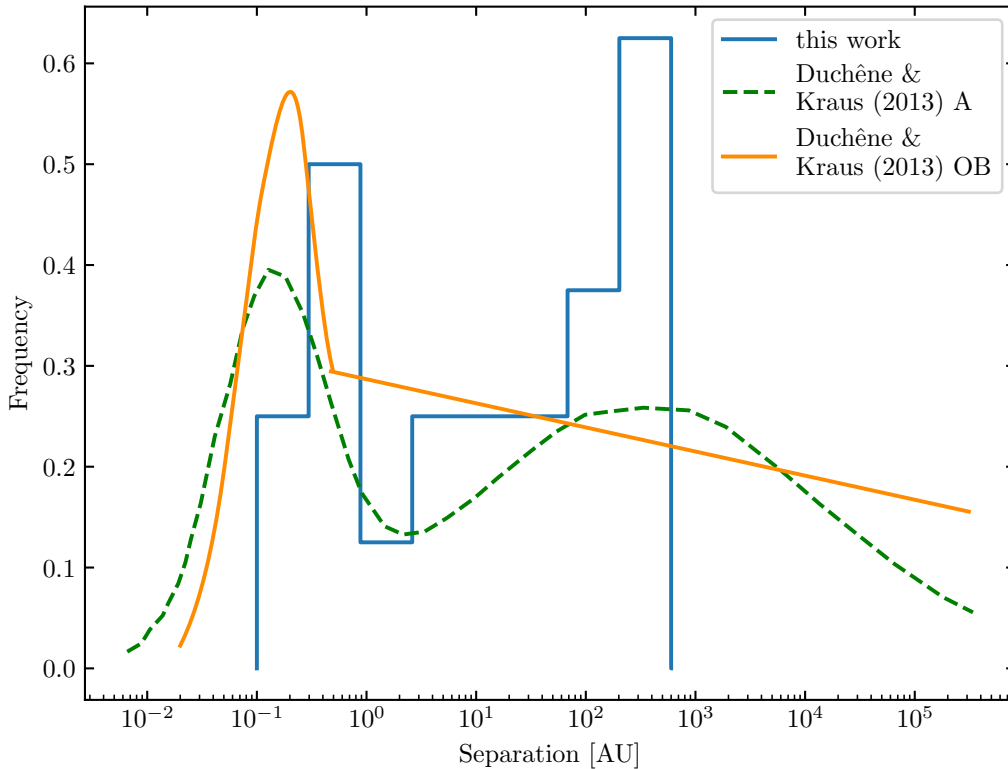
Fig. 24. Normalized histogram of companion separation. For comparison, we plot the qualitative distribution of Duchêne & Kraus (2013) for A (dotted) and OB stars (solid). The distribution of our separations for mainly B and O stars is bimodal and resembles more that of the Duchêne & Kraus (2013) distribution of A-type stars. We notice a decrease of companions in the range of 1–100 AU.
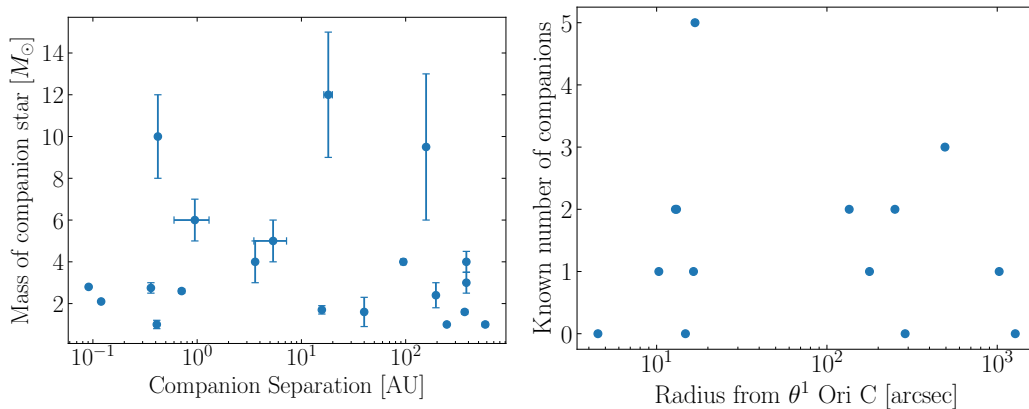
Fig. 25. Left: The separation versus the companion mass. Right: Multiplicity of objects plotted as a function of distance from θ^1 Ori C in arcseconds.

low mass companion is either ejected or evolves to a wide binary. The resulting system is a close high mass binary with a high mass companion and a third low mass component at larger separations (Bate et al. 2002). This preference for high mass companions also yields a top-heavy companion mass distribution. Another important factor is the low mass accretion rate of competitive accretion. Wang et al. (2010) showed that star formation with competitive accretion requires 10^6 yr when considering protostellar outflows and magnetic fields. Dynamical processes also need time to take place.

For massive star formation through stellar collisions/mergers, the stellar mass distribution does not result in a Salpeter IMF. The collisions lead to runaway growth of a few objects,

Parameter	Core accretion	Competitive accretion	Collisions	This work
CF	CF $\propto$ mass	CF $\propto$ mass	–	CF $\propto$ mass
IMF	top heavy	top heavy	strong deviation from Salpeter IMF	Salpeter IMF
m_2 and m_1	correlated	–	–	uncorrelated/ slightly correlated
r and M	correlated	$r \propto M^{-2}$	–	uncorrelated
q and r	–	anti-correlated	–	most $q \leq 0.5$ uncorrelated

Table 5. Comparison of observable quantities from the star formation models with our observations.

which does not produce a smooth mass distribution (Moeckel & Clarke 2011; Krumholz 2015). The collision of stars requires high densities $> 10^6$ stars/pc^3. Massive stars are a merger product and become less likely to be close binary systems (Bonnell & Bate 2005).

Our observations of the stars in the ONC yield a Salpeter IMF for all stars, including the companions. We do not observe massive binaries with equally massive companion stars. Also, we find no preference for close massive systems. The mass of the companion star is not correlated with the separation. We only find high mass ratios ($\gtrsim 0.5$) for primary stars with $\lesssim 7\ M_\odot$. In our sample, we observe fewer companions in the range of 1–100 AU. This indicates different formation mechanism for different separation ranges. This could be the transition of a mechanism responsible for tight binaries, e.g. failed mergers or accretion onto binaries, and e.g. disk fragmentation. Kratter & Lodato (2016) concluded that the disk of a star with $8\ M_\odot$ is sufficiently cool for fragmentation at ≥ 50 AU. This agrees with our gap between 1–10 AU and a slowly rising number of companions within 10–100 AU. Table 5 provides an overview of the various models and the predicted correlations. We compare the predictions with our findings.

We can exclude collisions as the main star formation process, because it does not represent our IMF and the density of the Trapezium ($\sim 10^4$ stars/pc^3 Hillenbrand & Hartmann 1998) is lower than the required $\sim 10^6$ stars/pc^3. θ^1 Ori C$_1$ might still be the result of stellar merging, but the collision of stars is not a dominant process in the ONC. We find several aspects in favor of competitive accretion in our sample, for example, the formation of massive stars at the cluster center and the variety of the mass range. However, other features do not support competitive accretion, e.g. we see no tight massive binaries or a preference for equal masses.

An important factor is that competitive accretion needs ~ 1 Myr to form massive stars (Wang et al. 2010; Portegies Zwart et al. 2010), whereas the ONC has an average age of < 1 Myr with a spread of less than 2 Myr. Core accretion provides a mechanism of gaining mass without tightening the binary separation. Both models have difficulties with reproducing our observations. However, we clearly do not find a strong dependence of binary separation with system mass $r \propto M^{-2}$ and an anti-correlation of mass ratios and separation. This argues against a dominant mode of competitive accretion. We also need to consider that some dynamic processes may not be completed yet, which could change the masses or companion fraction of the ONC.

Krumholz et al. (2012) showed in a simulation that a combination of core accretion and competitive accretion is also possible. Massive stars started formation in distinct massive cores, according to the core accretion model. But the formed stars engaged in dynamical interactions while accreting mass, similar to the competitive accretion model. This resulted

in hierarchical systems like the Trapezium Cluster. This combination could thus also be a possible scenario for the Trapezium, but needs further examination.

One has to note that both accretion scenarios initially form companions at large radii, which become eventually tight binaries, e.g. McKee & Ostriker (2007). This tightening process occurs through dynamical interactions with the disk or cluster members, or through ambient gas accretion and energy loss. It is therefore plausible that the observed fraction of close equal mass binaries depends on the cluster age. The ONC — with an age of 1 Myr (Hillenbrand 1997) — is one of the youngest massive star clusters in the Milky Way. Our finding of a large number of wide binaries with high mass ratios might reflect the fact that the binary population in the ONC did not have enough time to be altered by dynamical interactions e.g. (Moe & Kratter (2018) show different simulated scenarios of how close binaries can be formed, 60% form by unstable triples). Sana et al. (2017) also notice a lack of close companions and conclude their findings may support a theory in which binaries form initially at large separations and then harden to closer systems. This could explain why the companion separations and masses in the ONC are different than the distributions in more evolved clusters.

6. Conclusion

In order to gain a deeper understanding of massive star and cluster formation, this work presents an interferometric study of massive stars in the Orion Trapezium Cluster and its vicinity. The outstanding resolution of the VLTI ($\sim$2 mas) and the sensitivity of GRAVITY allowed us to probe stars for companions in the widely unexplored range of 1–100 AU. We observed the 16 most massive stars with masses of 2–44 $M_\odot$. We detected three new companions for the systems θ^1 Ori B, θ^2 Ori B, and θ^2 Ori C. We confirmed the suspected companion for NU Ori and determined a separation of 3.6 ± 0.1 AU. Combined with the companions reported in the literature — based on speckle/AO imaging and spectroscopic surveys –, we find a total of 22 companion stars. θ^1 Ori B$_6$ is at a separation of 3.5–7.2 AU and we estimated a mass of 7.3 ± 0.5 $M_\odot$. The new companion θ^2 Ori B$_2$ has a separation of 40 ± 1 AU and an approximate mass of 1.6 ± 0.7 $M_\odot$. For θ^2 Ori C$_2$ we determined a separation of 15.7 ± 0.2 AU and estimated a mass of 1.7 ± 0.2. NU Ori$_4$ has a separation of 3.6 ± 0.1 AU and an estimated mass of 4 ± 1 $M_\odot$.

We confirmed companions for θ^1 Ori A, θ^1 Ori C, θ^1 Ori D, and θ^2 Ori A, all with substantially improved astrometry and photometric mass estimates. Additionally, we refined the orbit of the eccentric high-mass binary θ^1 Ori C and obtained a period $P = 11.4 \pm 0.2$ yr and a semi-major axis $a = 18.2 \pm 0.3$ AU. Furthermore, we derived a new orbit for θ^1 Ori D with a semi-major axis $a = 0.77 \pm 0.03$ AU and a period $P = 53.03 \pm 0.06$ d. The system mass is 21.7 $M_\odot$, assuming a distance to the ONC of 414 ± 7 pc (Menten et al. 2007). We derived a multiplicity fraction of 0.69 and a companion fraction of 1.38 for our complete sample. Our observations are complete down to 3 $M_\odot$. We illustrate the observed companion systems in Figure 13.

The companion fraction rises with primary mass and extends from $\sim$0.6 for a mass range of $\leq$ 1–2 $M_\odot$ to 2.3 ± 0.3 for objects with $>$ 16 $M_\odot$. The multiplicity fraction also increases with object mass. We obtain a multiplicity fraction of 0.5 for objects with $\leq$ 1–2 $M_\odot$ and it rises up to 100% for stars with $>$ 16 $M_\odot$.

The companion mass distribution of our sample resembles an IMF with $N \propto m^{-2.3 \pm 0.3}$. We fit the distribution of the mass ratio q with a power law $\propto q^{-1.7 \pm 0.1}$. The exponent of the power law is smaller compared to previous findings. We did not observe a preference for twin binaries in any mass range and more specifically, there is no tendency for high-mass

stars to have companions of comparable masses in our sample. Additionally, we detected no correlation of the companion mass and the companion star separation.

We observed a bimodal distribution of the mass ratio q compared with the respective companion separation. This bimodal distribution resembles the distribution of A stars, even though our sample comprises mainly OB stars. We obtained a peak at separations $\sim$0.5 AU, followed by only few companions between 1–100 AU. This indicates a change of formation mechanism. Disk fragmentation becomes relevant at scales $\gtrsim$ 50 AU. Hence, the observations indicate a transition to companions formed by disk fragmentation. We found a second peak for separations $\geq$ 100 AU. Our sample covers separations up to $\sim$600 AU, thus we limit our conclusion to this separation range.

Finally, we compared our observational results with the expected properties of star formation models. We found no clear tendency for either core accretion or competitive accretion. There are several aspects contradicting the predictions of core accretion, competitive accretion and stellar collisions. We excluded stellar collisions as the main formation mechanism.

We notice fundamental differences between our observations and previous observations of star forming regions. The main differences are that the companion mass distribution follows a Salpeter IMF, and that we find no tendency for high-mass binaries with equal mass companions. The differences in stellar mass distribution could result from the improved sensitivity with long baseline interferometry and GRAVITY. Another explanation could be the very young age of Orion, which is too short for a dynamical evolution of its binary systems. Close systems, as often observed for O-type stars, have not yet formed in the ONC. Further similar studies of other star forming regions are necessary.

References

Absil, O., Le Bouquin, J.-B., Berger, J.-P., et al. 2011, A&A, 535, 10 pp.

Abt, H. A., Wang, R., & Cardona, O. 1991, Astrophys. J., 367, 155

Aikman, G. C. L. & Goldberg, B. A. 1974, JRASC, 68, 205

Allen, C., Costero, R., Ruelas-Mayorga, A., & Sánchez, L. J. 2017, Monthly Notices of the Royal Astronomical Society, 466, 4937

Allen, C. & Cox, A. 2000, Allen's Astrophysical Quantities, Allen's Astrophysical Quantities (Springer)

Astropy Collaboration, Robitaille, T. P., Tollerud, E. J., et al. 2013, A&A, 558, A33

Balega, I., Balega, Y. Y., Maksimov, A. F., et al. 2004, A&A, 422, 627

Balega, I. I., Balega, Y. Y., Maksimov, A. F., et al. 2007, Astrophys. Bull., 62, 339

Balega, Y. Y., Chentsov, E. L., Rzaev, A. K., & Weigelt, G. 2015, in Astronomical Society of the Pacific Conference Series, Vol. 494, Physics and Evolution of Magnetic and Related Stars, ed. Y. Y. Balega, I. I. Romanyuk, & D. O. Kudryavtsev, 57

Bally, J., Moeckel, N., & Throop, H. 2005, in Chondrites Protoplanetary Disk, Vol. 341, 81–106

Bastian, N., Covey, K. R., & Meyer, M. R. 2010, ARA&A, 48, 339

Bate, M. R., Bonnell, I. A., & Bromm, V. 2002, MNRAS, 336, 705

Bonnell, I. A. 2005a, in Astrophysics and Space Science Library, Vol. 327, The Initial Mass Function 50 Years Later, ed. E. Corbelli, F. Palla, & H. Zinnecker, 425

Bonnell, I. A. 2005b, in IAU Symposium, Vol. 227, Massive Star Birth: A Crossroads of Astrophysics, ed. R. Cesaroni, M. Felli, E. Churchwell, & M. Walmsley, 266–275

Bonnell, I. A. & Bate, M. R. 2005, MNRAS, 362, 915

Bonnell, I. A., Bate, M. R., Clarke, C. J., & Pringle, J. E. 1997, MNRAS, 285, 201

Bonnell, I. A., Bate, M. R., Clarke, C. J., & Pringle, J. E. 2001, MNRAS, 323, 785

Bonnell, I. A., Bate, M. R., & Vine, S. G. 2003, MNRAS, 343, 413

Bossi, M., Gaspani, A., Scardia, M., & Tadini, M. 1989, A&A, 222, 117

Bourgès, L., Mella, G., Lafrasse, S., & Duvert, G. 2013, ASPRO 2: Astronomical Software to PRepare Observations, Astrophysics Source Code Library

Bragança, G. A., Daflon, S., Cunha, K., et al. 2012, AJ, 144, 130

Briceño, C., Preibisch, T., Sherry, W. H., et al. 2007, Protostars Planets V, 345

Chabrier, G. 2003, PASP, 115, 763

Chelli, A., Duvert, G., Bourgès, L., et al. 2016, A&A, 589, A112

Chini, R., Hoffmeister, V. H., Nasseri, A., Stahl, O., & Zinnecker, H. 2012, Mon. Not. R. Astron. Soc., 424, 1925

Chini, R., Nasseri, A., Hoffmeister, V. H., Buda, L., & Barr, A. 2011, in Evol. Compact Bin. ASP Conf. Ser., ed. L. Schmidtobreick, M. Schreiber, & C. Tappert, Vol. 447, 67

Clarke, C. J. 2001, in IAU Symposium, Vol. 200, The Formation of Binary Stars, ed. H. Zinnecker & R. Mathieu, 346

Close, L. M., Males, J. R., Morzinski, K., et al. 2013, Astrophys. J., 774, 13pp

Close, L. M., Puglisi, A., Males, J. R., et al. 2012, Astrophys. J., 749, 1

Close, L. M., Wildi, F., Lloyd-Hart, M., et al. 2003, Astrophys. J., 599, 537

Corporon, P. & Lagrange, A.-M. 1999, Astron. Astrophys. Suppl. Ser., 136, 429

Costero, R., Allen, C., Echevarr, J., et al. 2008, in RevMexAA (Seria Conf., Vol. 34, 102–105

Costero, R., Echevarria, J., Richer, M. G., Poveda, A., & Li, W. 2006, IAU Circ., 8669

Cutri, R. M., Skrutskie, M. F., van Dyk, S., et al. 2003, VizieR Online Data Catalog, 2246

Da Rio, N., M., R., Hillenbrand, L. A., Henning, T., & Stassun, K. G. 2012, ApJ, 748, 14

Da Rio, N., Robberto, M., Soderblom, D. R., et al. 2010, ApJ, 722, 1092

de Wit, W. J., Testi, L., Palla, F., Vanzi, L., & Zinnecker, H. 2004, A&A, 425, 937

de Wit, W. J., Testi, L., Palla, F., & Zinnecker, H. 2005, A&A, 437, 247

Donati, J.-F., Babel, J., Harries, T. J., et al. 2002, MNRAS, 333, 55

Drass, H., Haas, M., Chini, R., et al. 2016, MNRAS, 461, 1734

Ducati, J. R. 2002, VizieR Online Data Catalog, 2237

Duchêne, G. & Kraus, A. 2013, Annu. Rev. Astron. Astrophys, 51, 269

Feigelson, E. D., Broos, P., Gaffney, III, J. A., et al. 2002, ApJ, 574, 258

Gaia Collaboration, Brown, A. G. A., Vallenari, A., et al. 2018, ArXiv e-prints [arXiv:1804.09365]

Gaia Collaboration, Prusti, T., de Bruijne, J. H. J., et al. 2016, A&A, 595, A1

Gallenne, A., Mérand, A., Kervella, P., et al. 2015, Astron. Astrophys., 579, 1

Genzel, R. & Stutzki, J. 1989, ARA&A, 27, 41

Gravity Collaboration, Abuter, R., Accardo, M., et al. 2017, A&A, 602, A94

Grellmann, R., Preibisch, T., Ratzka, T., et al. 2013, A&A, 550, 531

Grunhut, J. H., Wade, G. A., Neiner, C., et al. 2017, Monthly Notices of the Royal Astronomical Society, 465, 2432

Habibi, M., Gillessen, S., Martins, F., et al. 2017, ApJ, 847, 120

Hartwig, E. 1921, Astronomische Nachrichten, 212, 383

Herbig, G. H. 1950, Astrophys. J., 11, 15

Herbig, G. H. & Griffin, R. F. 2006, Astron. J., 132, 1763

Herrero, A., Kudritzki, R. P., Vilchez, J. M., et al. 1992, A&A, 261, 209

Hillenbrand, L. A. 1997, Astron. J., 113, 1733

Hillenbrand, L. A. & Hartmann, L. W. 1998, Astrophys. J., 492, 540

Houk, N. & Swift, C. 1999, in Michigan Spectral Survey, Ann Arbor, Dep. Astron., Univ. Michigan, Vol. 5

Kennicutt, R. C. 1998, Annu. Rev. Astron. Astrophys., 36, 189

Köhler, R., Petr-Gotzens, M. G., McCaughrean, M. J., et al. 2006, Astron. Astrophys., 458, 461

Kratter, K. & Lodato, G. 2016, Annual Review of Astronomy and Astrophysics, 54, 271

Kratter, K. M. & Matzner, C. D. 2006, MNRAS, 373, 1563

Kraus, S., Balega, Y. Y., Berger, J.-P., et al. 2007, A&A, 466, 649

Kraus, S., Weigelt, G., Balega, Y. Y., et al. 2009, a&a, 497, 195

Kroupa, P. 2001, MNRAS, 322, 231

Kroupa, P., Weidner, C., Pflamm-Altenburg, J., et al. 2013, The Stellar and Sub-Stellar Initial Mass Function of Simple and Composite Populations, ed. T. D. Oswalt & G. Gilmore (Dordrecht: Springer Netherlands), 115–242

Krumholz, M. R. 2006, ApJ, 641, L45

Krumholz, M. R. 2015, The Formation of Very Massive Stars, ed. J. S. Vink (Cham: Springer International Publishing), 43–75

Krumholz, M. R. 2016, Notes on Star Formation

Krumholz, M. R., Klein, R. I., & McKee, C. F. 2012, ApJ, 754, 71

Krumholz, M. R., Klein, R. I., Mckee, C. F., Offner, S. S. R., & Cunningham, A. J. 2009, Science (80-.)., 323, 754

Ku, W. H.-M., Righini-Cohen, G., & Simon, M. 1982, Science, 215, 61

Lada, C. J. & Lada, E. A. 2003, Annu. Rev. Astron. Astrophys, 41, 57

Landstreet, J. D., Kochukhov, O., Alecian, E., et al. 2017, A&A, 601, A129

Lapeyrere, V., Kervella, P., Lacour, S., et al. 2014, in Proc. SPIE, Vol. 9146, Optical and Infrared Interferometry IV, 91462D

Lawson, P. R. 2000, in Princ. Long Baseline Stellar Interferom., ed. P. R. Lawson

Lehmann, H., Vitrichenko, É. A., Bychkov, V., Bychkova, L., & Klochkova, V. 2010, Astron. Astrophys., 514, A34

Levato, H. & Abt, H. A. 1976, Publ. Astron. Soc. Pacific, 88, 712

Levenhagen, R. S. & Leister, N. V. 2006, MNRAS, 371, 252

Levesque, E. M., Massey, P., Olsen, K. A. G., et al. 2005, ApJ, 628, 973

Lohsen, E. 1975, Information Bulletin on Variable Stars, 988

Luri, X., Brown, A. G. A., Sarro, L. M., et al. 2018, ArXiv e-prints [arXiv:1804.09376]

Martins, F., Schaerer, D., & Hillier, D. J. 2005, Astron. Astrophys., 436, 1049

Mason, B. D., Gies, D. R., Hartkopf, W. I., et al. 1998, AJ, 115, 821

Mattei, J. & Baldwin, M. 1976, IAU Circ., 3004

McKee, C. F. & Ostriker, E. C. 2007, ARA&A, 45, 565

McKee, C. F. & Tan, J. C. 2002, Nature, 416, 59

Menten, K. M., Reid, M. J., Forbrich, J., & Brunthaler, A. 2007, a&a, 474, 515

Moe, M. & Di Stefano, R. 2017, ApJS, 230, 15

Moe, M. & Kratter, K. M. 2018, ApJ, 854, 44

Moeckel, N. & Clarke, C. J. 2011, MNRAS, 410, 2799

Morales-Calderón, M., Stauffer, J. R., Stassun, K. G., et al. 2012, Astrophys. J., 753, (17pp)

Morrell, N. & Levato, H. 1991, Astrophys. J. Suppl. Ser., 75, 965

Motte, F., Bontemps, S., & Louvet, F. 2018, Annu. Rev. Astron. Astrophys., 56, 1.1

Muench, A., Getman, K., Hillenbrand, L., & Preibisch, T. 2008, in Handb. Star Form. Reg., Vol. I, 483

Muench, A. A., Lada, E. A., Lada, C. J., & Alves, J. 2002, Astrophys. J., 573, 366

Mužić, K., Schödel, R., Scholz, A., et al. 2017, Monthly Notices of the Royal Astronomical Society, 471, 3699

Newville, M., Stensitzki, T., Allen, D. B., & Ingargiola, A. 2014, LMFIT: Non-Linear Least-Square Minimization and Curve-Fitting for Python

Nieva, M.-F. & Przybilla, N. 2014, Astron. Astrophys., 566, A7

O'Dell, C. R. & Wong, K. 1996, AJ, 111, 846

Oskinova, L. M., Steinke, M., Hamann, W.-R., et al. 2013, MNRAS, 436, 3357

Patience, J., Zavala, R. T., Prato, L., et al. 2008, ApJ, 674, L97

Peter, D., Feldt, M., Henning, T., & Hormuth, F. 2012, A&A, 538, A74

Petr, M. G., Coude du Foresto, V., Beckwith, S. V. W., Richichi, A., & McCaughrean, M. J. 1998, Astrophys. J., 500, 825

Popper, D. M. & Plavec, M. 1976, Astrophys. J., 205, 462

Portegies Zwart, S. F., McMillan, S. L. W., & Gieles, M. 2010, ARA&A, 48, 431

Preibisch, T., Balega, Y., Hofmann, K. H., Weigelt, G., & Zinnecker, H. 1999, New Astron., 4, 531

Reid, M. J., Menten, K. M., Brunthaler, A., et al. 2014, ApJ, 783, 130

Reiter, M., Calvet, N., Thanathibodee, T., et al. 2018, The Astrophysical Journal, 852, 5

Rio, N. D., Tan, J. C., Covey, K. R., et al. 2016, The Astrophysical Journal, 818, 59

Röser, S., Bastian, U., & Kuzmin, A. 1994, A&AS, 105, 301

Roy, A. E. 2005, Orbital motion, 4th edn. (Institute of Physics Publishing)

Salaris, M. & Cassisi, S. 2005, Evolution of Stars and Stellar Populations, 400

Salpeter, E. E. 1955, ApJ, 121, 161

Samus', N. N., Kazarovets, E. V., Durlevich, O. V., Kireeva, N. N., & Pastukhova, E. N. 2017, Astronomy Reports, 61, 80

Sana, H., de Mink, S. E., de Koter, A., et al. 2012, Science (80-.)., 337, 444

Sana, H., Le Bouquin, J.-B., Lacour, S., et al. 2014, ApJS, 215, 15

Sana, H., Ramírez-Tannus, M. C., de Koter, A., et al. 2017, A&A, 599, L9

Sanchez-Bermudez, J., Alberdi, A., Barbá, R., et al. 2017, ApJ, 845, 57

Scalo, J. M. 1986, Fundamentals of Cosmic Physics, 11, 1

Schertl, D., Balega, Y. Y., Preibisch, T., & Weigelt, G. 2003, Astron. Astrophys., 402, 267

Schneider, F. R. N., Sana, H., Evans, C. J., et al. 2018, Science, 359, 69

Schneller, H. 1948, Astronomische Nachrichten, 276, 144

Shu, F. H., Adams, F. C., & Lizano, S. 1987, ARA&A, 25, 23

Simon, M., Close, L. M., & Beck, T. L. 1999, Astron. J., 117, 1375

Simón-Díaz, S., Herrero, A., Esteban, C., & Najarro, F. 2006, Astron. Astrophys., 448, 351

Sota, A., Maíz Apellániz, J., Walborn, N. R., et al. 2011, ApJS, 193, 24

Stahl, O., Kaufer, A., Rivinius, T., et al. 1996, Astron. Astrophys., 312, 539

Stahl, O., Wade, G., Petit, V., Stober, B., & Schanne, L. 2008, Astron. Astrophys., 487, 323

Stahl, O., Wolf, B., Gang, T., et al. 1993, A&A, 274, L29

Stelzer, B., Flaccomio, E., Montmerle, T., et al. 2005, ApJS, 160, 557

Tan, J. C., Beltran, M. T., Caselli, P., et al. 2014, Protostars and Planets, VI, 149

Tatulli, E., Millour, F., Chelli, A., et al. 2007, A&A, 464, 29

The Astropy Collaboration, Price-Whelan, A. M., Sipőcz, B. M., et al. 2018, ArXiv e-prints [arXiv:1801.02634]

Vasileiskii, A. S. & Vitrichenko, É. A. 2000, Astron. Lett., 26, 529

Vitrichenko, É. A. 2002a, Astron. Lett., 12, 843

Vitrichenko, É. A. 2002b, Astron. Lett., 28, 324

Vitrichenko, É. A., Klochkova, V. G., & Plachinda, S. I. 1998, Astron. Lett., 24, 296

Vitrichenko, É. A., Klochkova, V. G., & Tsymbal, V. V. 2006, Astrophysics, 49, 96

Vitrichenko, É. A. & Plachinda, S. I. 2001, Astron. Lett., 27, 581

Voss, R., Diehl, R., Vink, J. S., & Hartmann, D. H. 2010, A&A, 520, A51

Wade, G. A., Fullerton, A. W., Donati, J.-F., et al. 2006, Astron. Astrophys., 451, 195

Wales, D. J. & Doye, J. P. K. 1997, J. Phys. Chem., 101, 5111

Wang, P., Li, Z.-Y., Abel, T., & Nakamura, F. 2010, ApJ, 709, 27

Weigelt, G., Balega, Y., Preibisch, T., et al. 1999, Astron. Astrophys., 347, L15

Wolff, S. C., Strom, S. E., & Hillenbrand, L. A. 2004, The Astrophysical Journal, 601, 979

Yorke, H. W. & Sonnhalter, C. 2002, ApJ, 569, 846

Zinnecker, H. & Yorke, H. W. 2007, Annu. Rev. Astron. Astrophys., 45, 481

[1] MPE - Max Planck Institute for extraterrestrial Physics, Giessenbachstr., 85741 Garching, Germany

[2] Department of Physics, Le Conte Hall, University of California, Berkeley, CA 94720, USA

[3] 1. Physikalisches Institut, Universität zu Köln, Zülpicher Str. 77, 50937 Köln, Germany

[4] European Southern Observatory, Karl-Schwarzschild-Str. 2, 85748 Garching, Germany

[5] CENTRA – Centro de Astrofísica e Gravitação, IST, Universidade de Lisboa, P-1049-001 Lisboa, Portugal; Universidade de Lisboa - Faculdade de Ciências, Campo Grande, 1749-016 Lisboa, Portugal

[6] CENTRA – Centro de Astrofísica e Gravitação, IST, Universidade de Lisboa, P-1049-001 Lisboa, Portugal; Faculdade de Engenharia, Universidade do Porto, Rua Dr. Roberto Frias, 4200-465 Porto, Portugal

[7] Univ. Grenoble Alpes, CNRS, IPAG, 38000 Grenoble, France

[8] Observatoire de Genève, Université de Genève, 51 Ch. des Maillettes, 1290 Versoix, Switzerland

[9] European Southern Observatory, Casilla 19001, Santiago 19, Chile

[10] MPIA - Max-Planck-Institut für Astronomie, Königstuhl 17, 69117, Heidelberg, Germany

[11] LESIA - Observatoire de Paris, Université PSL, CNRS, Sorbonne Université, Univ. Paris Diderot, Sorbonne Paris Cité, 5 place Jules Janssen, 92195 Meudon, France

[12] Sterrewacht Leiden, Leiden University, Postbus 513, 2300 RA Leiden, The Netherlands

[13] Max-Planck-Institute for Radio Astronomy, Auf dem Hügel 69, 53121 Bonn, Germany

[14] ESA - European Space Agency, Space Telescope Science Institute, 3700 San Martin Drive, Baltimore MD 21218, USA

[15] Dublin Institute for Advanced Studies, Astronomy & Astrophysics Section, 31 Fitzwilliam Place, D02 XF86, Dublin, Ireland

[16] University of Vienna, Universitätsring 1, 1010 Wien, Austria

Appendix A: Data Results

We present our resulting separations and flux ratios for object. We list the values for θ^1 Ori A and θ^1 Ori C that we took from the literature as well, but in separate tables.

Appendix A.1: θ^1 Ori A

Date	MJD	x [mas]	Δ x	y [mas]	Δy	f	Δf
2016.900	57717.34	37.84	0.06	177.55	0.09	0.240	0.006
2017.779	58038.38	40.6	0.1	175.1	0.3	0.34	0.05
2017.779	58038.39	40.69	0.09	175.1	0.2	0.36	0.05
2018.031	58130.16	41.55	0.04	174.49	0.07	0.230	0.008
2018.031	58130.16	41.70	0.04	174.25	0.06	0.209	0.007

Table A.1. Results of the binary fit for GRAVITY data of θ^1 Ori A. Relative positions x and y in respect to the primary star, with x pointing towards the east and y towards the north. The uncertainties are Δx and Δy. f is the resulting flux ratio, Δf the uncertainty. The first column lists the Date and the second column the MJD of the observation.

Date	MJD	PA [°]	ΔPA [°]	Sep[mas]	Δ Sep [mas]	Reference
1995.775	50001.319	350.6	2	227	5	[1]
1996.247	50173.717	352.8	2	227	4	[1]
1996.746	50355.977	352.7	2	223	4	[1]
1997.788	50736.567	353	2	224	2	[1]
1998.838	51120.080	353.8	2	221	5	[1]
1998.841	51121.175	353.8	2	221.5	5	[2]
1999.715	51440.404	355.4	2	219	3	[1]
1999.737	51448.439	354.8	2	215	3	[1]
1999.819	51478.390	355.1	0.5	212	2.5	[3]
2000.765	51823.916	356.2	2	215	4	[1]
2000.781	51829.760	356.1	2	216	4	[1]
2000.781	51829.760	356	2	215	3	[1]
2001.186	51977.687	356	2	215	3	[1]
2001.718	52172.000	356.9	1	205.1	3	[4]
2003.701	52896.290	3.9	1	210	5	[5]
2003.945	52985.411	3.9	1	209	5	[5]
2004.816	53303.544	0.3	1.6	203	2	[6]
2004.822	53305.736	0.9	0.8	205	3	[6]
2004.945	53350.661	4.6	1	207	5	[5]
2005.06	53392.665	5.3	1	208	5	[5]
2005.94	53714.085	5.9	1	204	5	[5]
2007.704	54358.386	6.1	1	202	5	[5]
2009.019	54838.690	7.5	1	199	5	[5]
2009.885	55154.996	8.2	1	197	5	[5]
2009.899	55160.110	8.5	1	198	5	[5]
2010.26	55291.965	9.4	1	197	5	[5]
2010.877	55517.324	6.5	0.3	193.1	0.5	[4]
2010.953	55545.083	6.2	2	193	1	[5]
2011.827	55864.312	7.3	2	193.2	1	[5]

Table A.2. Positions of θ^1 Ori A$_2$, in position angle (PA) and separation (Sep) with respect to the primary star. The observation time is listed in the first column. The corresponding uncertainties are denoted as ΔPA and ΔSep Positions are taken from indicated references: [1] Schertl et al. (2003), [2] Weigelt et al. (1999), [3] Balega et al. (2004), [4] Close et al. (2012), [5] Grellmann et al. (2013), [6] Balega et al. (2007).

Appendix A.2: θ^1 Ori B

Date	MJD	x	Δ	y	Δy	f	Δf
2017.028	57764.11	-7.10	0.02	-4.68	0.02	0.224	0.003
2017.138	57804.11	-8.64	0.03	-4.5	0.1	0.30	0.01
2017.209	57830.03	-9.656	0.002	-4.304	0.002	0.325	0.001
2017.217	57833.03	-9.897	0.002	-4.196	0.002	0.330	0.005
2017.777	58037.38	-15.841	0.003	-2.081	0.007	0.442	0.002
2017.779	58038.35	-15.763	0.004	-2.136	0.008	0.296	0.001
2017.782	58039.38	-15.841	0.003	-2.081	0.007	0.442	0.002
2017.782	58039.4	-15.821	0.004	-2.104	0.007	0.453	0.003
2018.028	58129.12	-17.212	0.003	-0.987	0.005	0.303	0.001

Table A.3. Results of the binary fit for GRAVITY data of θ^1 Ori B. Relative positions x and y in respect to the primary star, with x pointing towards the east and y towards the north. The uncertainties are Δx and Δy. f is the resulting flux ratio, Δf the uncertainty. The first column lists the observation time and the second column the MJD of the observation.

Appendix A.3: θ^1 Ori C

Date	MJD	x	Δx	y	Δy	f	Δf
2015.854	57335.34	6.53	0.03	26.23	0.030	0.266	0.002
2016.021	57396.23	5.572	0.003	25.217	0.006	0.296	0.001
2016.758	57665.36	0.368	0.003	19.243	0.008	0.285	0.002
2016.900	57717.21	-0.616	0.007	17.841	0.007	0.27	0.002
2017.209	57830.05	-2.751	0.009	14.726	0.007	0.309	0.002
2017.776	58037.34	-6.85	0.03	8.67	0.05	0.29	0.04
2017.779	58038.32	-6.92	0.02	8.57	0.02	0.41	0.03
2018.031	58130.2	-8.346	0.007	5.97	0.01	0.307	0.002

Table A.4. Results of the binary fit for GRAVITY data of θ^1 Ori C. Relative positions x and y in respect to the primary star, with x pointing towards the east and y towards the north. The uncertainties are Δx and Δy. f is the resulting flux ratio, Δf the uncertainty. The first column lists the observation time and the second column the MJD of the observation.

Date	MJD	PA [deg]	Δ PA [deg]	Sep [mas]	Δ Sep [mas]	Reference
1997.784	50735.106	226	3	33	2	[1]
1998.383	50953.891	222	5	37	4	[1]
1999.737	51448.439	214	2	43	1	[2]
1999.819	51478.353	213.5	2	42	1	[3]
2000.873	51863.509	210	2	40	1	[3]
2001.184	51976.956	208	2	38	1	[2]
2003.8	52932.450	19.3	2	29	2	[3]
2003.925	52978.252	19	2	29	2	[3]
2003.928	52979.202	19.1	2	29	2	[3]
2004.822	53305.589	10.5	4	24	4	[3]
2005.921	53706.981	342.74	2	13.55	0.5	[3]
2006.149	53790.276	332.3	3.5	11.8	1.11	[4]
2007.019	54108.263	274.9	1	11.04	0.5	[5]
2007.143	54153.298	268.1	5.2	11.94	0.31	[4]
2007.151	54156.293	272.9	8.8	12.13	1.58	[4]
2007.175	54165.278	266.6	2.1	12.17	0.37	[4]
2007.206	54176.309	265.6	1.9	12.28	0.41	[4]
2007.214	54179.304	263	2.3	12.14	0.43	[4]
2007.901	54430.486	238	2	19.8	2	[5]
2007.923	54438.485	241.2	1	19.07	0.5	[5]
2008.027	54476.508	237	3	19.7	3	[5]
2008.027	54476.508	236.5	3	19.6	3	[5]
2008.071	54492.506	236.2	2	20.1	2	[5]
2008.148	54520.520	234.6	1	21.17	0.5	[5]
2008.173	54529.542	236.4	1	21.27	0.5	[5]
2010.762	55475.321	216.3	2	42.6	1	[6]
2010.986	55557.137	215.7	2	43.4	1	[6]
2010.989	55558.232	215	2	43.1	1	[6]

Table A.5. Positions of θ^1 Ori C_2, in position angle (PA) and separation (Sep) with respect to the primary star. The first column lists the observation time and the second column the MJD of the observation. The corresponding uncertainties are denoted as ΔPA and ΔSep Positions are taken from indicated references: [1] Weigelt et al. (1999), [2] Schertl et al. (2003), [3] Kraus et al. (2007), [4] Patience et al. (2008), [5] Kraus et al. (2009), [6] Grellmann et al. (2013).

Appendix A.4: θ^1 Ori D

Date	MJD	x	Δx	y	Δy	f	Δf
2016.903	57718.315	-0.967	0.01	2.378	0.02	0.422	0.012
2017.212	57831.052	-1.571	0.004	1.4	0.005	0.365	0.002
2017.217	57833.005	-1.576	0.02	0.98	0.02	0.331	0.01
2017.217	57833.005	-1.614	0.007	1.01	0.01	0.349	0.003
2017.782	58039.332	-1.27	0.01	1.95	0.02	0.295	0.006
2018.025	58128.128	0.881	0.004	2.315	0.008	0.338	0.002
2018.030	58130.094	0.662	0.002	2.477	0.004	0.335	0.001

Table A.6. Results of the binary fit for GRAVITY data of θ^1 Ori D. Relative positions x and y in respect to the primary star, with x pointing towards the east and y towards the north. The uncertainties are Δx and Δy. f is the resulting flux ratio, Δf the uncertainty. The first column lists the observation time and the second column the MJD of the observation.

Appendix A.5: θ^2 Ori A

Date	MJD	x	Δx	y	Δy	f	Δf
2016.903	57718.263	0.36	0.01	-1.21	0.02	0.53	0.06
2018.030	58130.111	-0.062	0.002	0.993	0.008	0.52	0.02
2018.031	58130.157	-0.291	0.002	0.946	0.005	0.72	0.04

Table A.7. Results of the binary fit for GRAVITY data of θ^2 Ori A. Relative positions x and y in respect to the primary star, with x pointing towards the east and y towards the north. The uncertainties are Δx and Δy. f is the resulting flux ratio, Δf the uncertainty. The first column lists the MJD of the observation.

Appendix A.6: θ^2 Ori B

We observed θ^2 Ori B on January 10th 2018 with: $x = -66.93 \pm 0.04$, $y = 68.52 \pm 0.07$, $f = 0.022 \pm 0.001$.

Appendix A.7: θ^2 Ori C

We observed θ^2 Ori C on January 12th 2018 with: $x = -36.74 \pm 0.02$, $y = 10.21 \pm 0.03$, $f = 0.114 \pm 0.002$.

Appendix A.8: NU Ori

Date	MJD	x	Δx	y	Δy	f	Δf
2017.782	58039.3443	-8.480	0.007	1.07	0.01	0.179	0.001
2018.025	58128.0987	-2.695	0.005	3.46	0.01	0.189	0.001

Table A.8. Results of the binary fit for GRAVITY data of NU Ori. Relative positions x and y in respect to the primary star, with x pointing towards the east and y towards the north. The uncertainties are Δx and Δy. f is the resulting flux ratio, Δf the uncertainty. The first column lists the date and the second column the MJD of the observation.

Object	Date [UT]	Spectral resolution	Baseline configuration	DIT [s]	NDIT
θ^1 Ori A	2016 Nov 25	Medium	K0 G2 D0 J3	10	60
θ^1 Ori A	2017 Oct 12	Medium	A0 G1 J2 K0	5	120
θ^1 Ori A	2018 Jan 12	Medium	A0 G1 J2 K0	5	120
θ^1 Ori B	2017 Jan 11	Medium	U1 U2 U3 U4	5	100
θ^1 Ori B	2017 Feb 20	Medium	A0 G1 J2 K0	10	25
θ^1 Ori B	2017 Mar 18	Medium	A0 G1 J2 J3	10	50
θ^1 Ori B	2017 Mar 20	Medium	A0 G1 J2 K0	10	100
θ^1 Ori B	2017 Mar 21	Medium	A0 G1 J2 K0	10	50
θ^1 Ori B	2017 Oct 11	Medium	A0 G1 J2 K0	5	240
θ^1 Ori B	2017 Oct 12	Medium	A0 G1 J2 K0	5	120
θ^1 Ori B	2017 Oct 13	Medium	A0 G1 J2 K0	5	240
θ^1 Ori B	2018 Jan 11	Medium	A0 G1 J2 K0	5	120
θ^1 Ori C	2015 Nov 09	Medium	A0 B2 D0 C1	3	200
θ^1 Ori C	2016 Jan 09	Medium	A0 G1 J2 K0	3	400
θ^1 Ori C	2016 Oct 04	Medium	A0 G1 J2 K0	10	45
θ^1 Ori C	2016 Oct 04	Low	A0 G1 J2 K0	1	240
θ^1 Ori C	2016 Oct 04	Low	A0 G1 J2 K0	0.3	200
θ^1 Ori C	2016 Nov 25	Medium	K0 G2 D0 J3	10	30
θ^1 Ori C	2017 Mar 18	Medium	A0 G1 J2 J3	10	50
θ^1 Ori C	2017 Oct 11	Medium	A0 G1 J2 K0	5	120
θ^1 Ori C	2017 Oct 12	Medium	A0 G1 J2 K0	5	120
θ^1 Ori C	2018 Jan 12	Medium	A0 G1 J2 K0	5	120
θ^1 Ori D	2016 Nov 26	Medium	K0 G2 D0 J3	10	30
θ^1 Ori D	2017 Mar 19	Medium	A0 G1 J2 K0	10	60
θ^1 Ori D	2017 Mar 21	Medium	A0 G1 J2 K0	10	50
θ^1 Ori D	2017 Oct 13	Medium	A0 G1 J2 K0	5	120
θ^1 Ori D	2018 Jan 10	Medium	A0 G1 J2 K0	5	120
θ^1 Ori D	2018 Jan 10	Medium	A0 G1 J2 K0	5	120
θ^1 Ori E	2017 Mar 20	Medium	A0 G1 J2 K0	10	50
θ^1 Ori F	2016 Jan 10	Medium	A0 G1 J2 K0	30	30
θ^1 Ori F	2016 Jan 17	Medium	A0 G1 J2 K0	30	10
θ^1 Ori F	2016 Jan 21	Medium	A0 G1 J2 K0	30	40
θ^1 Ori F	2017 Jan 29	Medium	A0 G1 J2 K0	30	10
θ^1 Ori F	2017 Jan 30	Medium	A0 G1 J2 K0	30	10
θ^2 Ori A	2016 Nov 26	Medium	K0 G2 D0 J3	10	30
θ^2 Ori A	2018 Jan 10	Medium	A0 G1 J2 K0	5	120
θ^2 Ori A	2018 Jan 12	Medium	A0 G1 J2 K0	5	120
θ^2 Ori B	2018 Jan 10	Medium	A0 G1 J2 K0	5	120
θ^2 Ori C	2018 Jan 12	Medium	A0 G1 J2 K0	5	120
NU Orionis	2017 Oct 13	Medium	A0 G1 J2 K0	5	120
NU Orionis	2018 Jan 10	Medium	A0 G1 J2 K0	5	120
LP Ori	2018 Jan 11	Medium	A0 G1 J2 K0	5	120
Brun 862	2018 Jan 11	Medium	A0 G1 J2 K0	5	120
HD 37115	2018 Jan 11	Medium	A0 G1 J2 K0	5	120
HD 37150	2018 Jan 11	Medium	A0 G1 J2 K0	5	120
TCC 59	2018 Jan 04	Low	A0 G1 J2 K0	10	60

Table 1 — continued from previous page

Object	Date [UT]	Spectral resolution	Baseline configuration	DIT [s]	NDIT
TCC 59	2018 Jan 05	Low	A0 G1 J2 K0	10	60
TCC 43	2018 Jan 04	Low	A0 G1 J2 K0	10	30

Table 1. GRAVITY observations of the Orion Nebula. From left to right: name of the observed object, observation date, spectral resolution, baseline configuration, and the integration time (DIT) with the number of integrations (NDIT) .

Object	Component	Sep [AU]	Period	Spec. type	m_K	Mass [$M_\odot$]	Limit [$M_\odot$]	Reference
θ^1 Ori A	**A_1**			**B0.5V**	**5.67**	**14 ± 5**		[1, 2, 3]
	A_2	**90 −100**	**214 yr**	**F PMS**	**7.3 ± 0.3**	**4**		[This work, 4, 5, 6, 10, 26]
	A_3	0.71	65.09 ± 0.07 d	T Tauri		2.6 ± 0.1		[7, 8, 9, 11, 12, 13]
θ^1 Ori B	**B_1**			**B1V**	**6.00**	**7.2 ± 0.2**	**< 1.9**	[This work, 2, 16, 22, 33]
	B_2	382 ± 6	1920 yr		7.6	4		[4, 5, 10, 26]
	B_3	49 ± 1	200 yr		8.6	3		[4, 5, 10, 26]
	B_4	248 ± 4	2000 ± 700 yr		11.66	1		[15, 26, 32, 42]
	B_5	0.120 ± 0.002	6.47 d			2		[13, 14, 26]
	B_6	**3.5-7.2**		**B**	**7.3 ± 0.5**	**4 −6**		[This work, 19]
θ^1 Ori C	**C_1**			**O7V**	**4.57**	**33.5 ± 5.2**	**< 3**	[This work, 17, 18, 20, 21, 45]
	C_2	**18.1 ± 1.7**	**11.4 yr**	**O9.5**	**6.0 ± 0.4**	**12 ± 3**		[This work, 5, 7, 20, 21, 22, 23]
	$C_3.$	0.41 ± 0.01	61.49 d			1.0 ± 0.2		[23, 24]
θ^1 Ori D	**D_1**			**B1.5V**	**5.75**	**16 ± 1**	**< 2.8**	[2, 3, 27]
	D_2	580 ± 10			11.69 ± 0.06	1 ± 0.1		[This work, 26]
	D_3	**0.77 ± 0.03**	**53.03 ± 0.07 d**	**B**	**6.9 ± 0.3**	**6 ± 1**		[This work, 6, 25, 43]
θ^1 Ori E	**E_1**			**G2IV**	**6.9**	**2.81 ± 0.05**	**< 1.8**	[28, 29, 30, 31]
	E_2	0.091 ± 0.001	9.8952 ± 0.0007 d	G0IV −G5III		2.80 ± 0.05		[28, 30, 31]
θ^2 Ori A	**A_1**			**O9.5IV**	**4.94**	**39 ± 14**	**< 1.6**	[3, 17, 18]
	A_2	**0.42 ± 0.01**	**20.974 ± 0.003 d**		**5.7 ± 0.2**	**10 ± 2**		[This work, 13]
	A_3	157				6–13		[16, 32]
θ^2 Ori B	**B_1**			**B2 −B5**	**6.41**	**14.8 ± 3.4**	**< 1.9**	[3, 18, 33, 34]
	B_2	**40 ± 1**		**A −F**	**10.6 ± 1.3**	**1.6 ± 0.7**		[This work]
θ^2 Ori C	**C_1**			**B5V**	**7.54**	**4 ± 1**		[2, 39]
	C_2	0.165 ± 0.003	13 d					[35]
	C_3	**15.7 ± 0.2**		**A**	**9.89 ± 0.07**	**1.7 ± 0.2**		[This work]
NU Ori	**NU Ori$_1$**			**O9V**	**5.49**	**16 ± 3**	**< 2**	[2, 6, 33, 37]
	NU Ori$_2$	0.36 ± 0.01	19.1387 ± 0.0028 d			> 2.5		[This work, 13]
	NU Ori$_3$	195 ± 4		A or B	8.7 ± 0.1	2.4 ± 0.6		[This work, 32, 36]
	NU Ori$_4$	**3.6 ± 0.1**		**B**	**7.3 ± 0.1**	**4 ± 1**		[This work]
HD 37115	**HD 37115$_1$**			**B5**	**7.13**	**5.4 ± 0.4**	**< 2.2**	[This work, 2, 32, 40]

Table 4 — Continued on next page

Table 4 — continued from previous page

Object	Component	Sep [AU]	Period	Spec. Type	m_{K}	Mass [$M_\odot$]	Limit [$M_\odot$]	Reference
	HD 37115$_2$	368 ± 6				1.6 ± 0.1		[32]
TCC 59	**TCC 59$_1$**			**YSO**	**11.05**	**≥ 1.5**		[This work, 29]
	TCC 59$_2$	56 ± 2						[26]
Brun 862				**K3-M0I**	**4.49**	**13**	**< 2.2**	[This work, 2, 33]
θ^1 **Ori F**				**B8**	**8.38**	**2.2 −2.8**	**< 1.5**	[This work, 29, 38]
TCC 43				**A −F**	**10.44**	**> 1.5 −1.7**	**< 1.1**	[This work, 29]
LP Ori				**B1.5V**	**7.47**	**6.70** $^{+0.64}_{-0.37}$	**< 1.9**	[This work, 2, 33, 39, 44]
HD 37150				**B3III/IV**	**7.11**	**≥ 7**	**< 1.9**	[This work, 2, 41]

Table 4. Overview for all the observed stars. From left to right starting with the object, its component, the separation or, if known, the semi-major axis, the period, spectral type, magnitude in K-band, mass of component, detection limit and the reference. Objects in bold have been observed with GRAVITY. The uncertainties for the mass are taken from the literature. Values without uncertainties are not necessarily exact but were published without an error estimate.

References: [1] Levato & Abt (1976), [2] Cutri et al. (2003), [3] Simón-Díaz et al. (2006), [4] Petr et al. (1998), [5] Schertl et al. (2003), [6] Grellmann et al. (2013), [7] Mattei & Baldwin (1976), [8] Lohsen (1975), [9] Bossi et al. (1989), [10] Close et al. (2003), [11] Vitrichenko et al. (1998), [12] Vitrichenko & Plachinda (2001), [13] Abt et al. (1991), [14] Popper & Plavec (1976), [15] Simon et al. (1999), [16] Mason et al. (1998), [17] Sota et al. (2011), [18] Ducati (2002), [19] Vasileiskii & Vitrichenko (2000), [20] Kraus et al. (2007), [21] Kraus et al. (2009), [22] Weigelt et al. (1999), [23] Lehmann et al. (2010), [24] Vitrichenko (2002b), [25] Vitrichenko (2002a), [26] Close et al. (2012), [27] Levenhagen & Leister (2006), [28] Herbig & Griffin (2006), [29] Muench et al. (2002), [30] Morales-Calderón et al. (2012), [31] Costero et al. (2008), [32] Preibisch et al. (1999), [33] Hillenbrand (1997), [34] Nieva & Przybilla (2014), [35] Corporon & Lagrange (1999), [36] Köhler et al. (2006), [37] Bragança et al. (2012), [38] Herbig (1950), [39] Samus' et al. (2017), [40] Röser et al. (1994), [41] Houk & Swift (1999), [42] Close et al. (2013), [43] Allen et al. (2017), [44] Reiter et al. (2018), [45] Balega et al. (2015)